

## THE ORBITAL STRUCTURE OF TRIAXIAL GALAXIES WITH FIGURE ROTATION

ALEX T. DEIBEL,<sup>1,2</sup> MONICA VALLURI,<sup>1</sup> AND DAVID MERRITT,<sup>3</sup>

*Draft version November 9, 2018*

### ABSTRACT

We survey the properties of all orbit families in the rotating frame of a family of realistic triaxial potentials with central supermassive black holes (SMBHs). In such galaxies, most regular box orbits (vital for maintaining triaxiality) are associated with resonances which occupy two-dimensional surfaces in configuration space. For slow figure rotation all orbit families are largely stable. At intermediate pattern speeds a significant fraction of the resonant box orbits as well as inner long-axis tubes are destabilized by the “envelope doubling” that arises from the Coriolis forces and are driven into the destabilizing center. Thus, for pattern rotation periods  $2 \times 10^8 \text{ yr} \lesssim T_p \lesssim 5 \times 10^9 \text{ yr}$ , the two orbit families that are most important for maintaining triaxiality are highly chaotic. As pattern speed increases there is also a sharp decrease in the overall fraction of prograde short-axis tubes and a corresponding increase in the retrograde variety. At the highest pattern speeds (close to that of triaxial bars), box-like orbits undergo a sudden transition to a new family of stable retrograde loop-like orbits, which resemble orbits in three-dimensional bars, and circulate about the short axis. Our analysis implies that triaxial systems (with central cusps and SMBHs) can either have high pattern speeds like fast bars or low pattern speeds like triaxial elliptical galaxies or dark matter halos found in  $N$ -body simulations. Intermediate pattern speeds produce a high level of stochasticity in both the box and inner long-axis tube orbit families implying that stable triaxial systems are unlikely to have such pattern speeds.

### 1. INTRODUCTION

It is widely accepted that since both elliptical galaxies and dark matter halos form via hierarchical mergers, they should be triaxial. If a significant amount of gas is present in the progenitor galaxies, its dissipative condensation generally results in systems that are more oblate than those produced in purely collisionless collapse (Dubinski 1994; Kazantzidis et al. 2004; Debattista et al. 2008). However, recent studies have shown that two orbit families that characterize triaxial systems (boxes and long-axis tubes) persist in significant numbers even when a triaxial system *looks* almost oblate (van den Bosch & de Zeeuw 2010; Valluri et al. 2010). Since merging systems generally have angular momentum (either internal angular momentum of the individual progenitors or the angular momentum of their relative orbit or both), merger remnants generally have angular momentum. If the remnants are triaxial, they can exhibit figure rotation: a property that is independent of the streaming motions of individual particles.

Although it is logical to assume that triaxial elliptical galaxies can have figure rotation, it is currently difficult (if not impossible) to observationally distinguish between figure rotation (tumbling) and orbital streaming. Although figure rotation was first proposed to explain “anomalous dust lanes” in triaxial elliptical galaxies (van Albada et al. 1982), there have been only a few observational attempts to measure the pattern speeds of either elliptical galaxies or dark matter halos (Bureau et al. 1999; Jeong et al. 2007). Cosmological  $N$ -body simulations (without dissipation) predict that dark matter halos are significantly triaxial and that a majority of dark matter halos ( $\sim 90\%$ ) have figure rotation (Bailin & Steinmetz 2004;

Bryan & Cress 2007) with slow pattern speeds following a lognormal distribution centered on  $\Omega_p = 0.148 h \text{ km s}^{-1} \text{ kpc}^{-1}$ . Bailin & Steinmetz (2004) found that the pattern speed of the figure rotation is correlated with the cosmological halo spin parameter  $\lambda$  (Peebles 1969), but is independent of halo mass. Figure rotation of triaxial dark matter halos has been suggested as a mechanism for driving spiral structure, warps and bars in spiral and elliptical galaxies with low mass disks (Bureau et al. 1999; Dubinski & Chakrabarty 2009). The only family of triaxial stellar systems with strong figure rotation is the bars of spiral and lenticular galaxies. Rapidly rotating (triaxial) bars can be almost completely regular (Pfenniger & Friedli 1991) and have a complex orbital structure (Skokos et al. 2002a,b; Patsis et al. 2002; Harsoula & Kalapotharakos 2009).

Emsellem et al. (2007) introduced a luminosity weighted measure of the specific line-of-sight angular momentum,  $\lambda_R$ , to quantify the angular momentum content of E/S0 galaxies observed in the SAURON sample. They found that this parameter allows E/S0 galaxies to be classified into two subgroups – the “fast rotators” with  $\lambda_R > 0.1$  and “slow rotators” with  $\lambda_R < 0.1$ . The slow rotators are likely to be triaxial ellipticals since they frequently display isophotal and kinematic twists, including kinematically decoupled cores. They tend to be more luminous and have shallow central cusps (Emsellem et al. 2007; Cappellari et al. 2007). In contrast, “fast rotators” are more numerous and close to axisymmetric, but may retain a significant population of triaxial orbit families such as box and long-axis tube orbits (van den Bosch & de Zeeuw 2010). These authors find that even a small fraction of box-like orbits can significantly alter the dynamical estimates of supermassive black hole (SMBH) masses. Recent  $N$ -body simulations of mergers of gas rich disk galaxies that include star formation and dissipation show that both fast and slow rotators can be formed in mergers between disk galaxies. The latter class primarily form in major mergers with smaller gas fractions and are more triaxial (Jesseit et al. 2009). (Recently, Bois

<sup>1</sup> Department of Astronomy, University of Michigan, Ann Arbor, MI 48109, USA [mvalluri@umich.edu](mailto:mvalluri@umich.edu)

<sup>2</sup> Department of Physics and Astronomy, Michigan State University, East Lansing MI, 48824, USA

<sup>3</sup> Department of Physics and Center for Computational Relativity and Gravitation, Rochester Institute of Technology, 84 Lomb Memorial Dr., Rochester, NY 14623, USA

et al. (2010) have shown that due to numerical resolution effects in  $N$ -body simulations, the fraction of merger remnants that are triaxial slow rotators may have been underestimated). Thus despite the absence of concrete observational measurements, some fraction of triaxial elliptical galaxies and dark matter halos could have figure rotation.

There has been little work on the effects of figure rotation on triaxial galaxies in the last two decades – none on realistic density profiles with central cusps and SMBHs. Binney (1981) studied the effect of figure rotation on the behavior of the closed periodic orbits in the equatorial plane perpendicular to the axis of rotation ( $z$ ) of flattened galaxy models including those with weak bars. He showed that closed retrograde orbits in the  $x$ - $y$  plane lying in an annular region (now called the “Binney instability strip”) become unstable to perturbations perpendicular to the plane. He also showed that this instability strip moved inward as the speed of rotation of the figure increased.

Heisler et al. (1982) studied the stability of closed orbits in a triaxial model with a central density core subjected to both slow (pattern rotation period  $T_p \sim 10^9$  yr) and fast rotations ( $T_p \sim 10^8$  yr). They showed that the 1:1 periodic orbits that circulate about the long ( $x$ ) axis of the model are stable to figure rotation and are tipped about the  $y$ -axis by the Coriolis forces in a direction that depends on their sense of motion. Two such orbits exist: one rotates clockwise about the  $x$ -axis and the other circulates anti-clockwise. However, both “tipped” orbits circulated about the short axis in the same direction. (These orbits were termed “anomalous” by van Albada et al. (1982).) The long-axis tube family that is “parented” by the anomalous orbits was therefore also expected to be stable and also “tipped” at an angle. They noted that for orbits with very large energies (i.e., extending to large radii) such orbits could be tipped by  $\sim 90^\circ$  into the equatorial plane. Our more general analysis in models with realistic density profiles shows that while outer long-axis tubes indeed behave as predicted, the inner long-axis tubes with the small pericentric radii are easily destabilized by figure rotation (Section 3.2).

Heisler et al. (1982) also showed that the normal retrograde orbits that lie in the equatorial plane were stable (except in the Binney instability strip, where they were unstable to vertical perturbations). The sequence of closed, stable period orbits identified by them were found to exist at both slow and fast pattern speeds and constituted one composite sequence which was stable over the entire energy range. They speculated that this implied that triaxial galaxies could have both fast and slow pattern speeds.

de Zeeuw & Merritt (1983) complemented this work, with a study of orbits in the principal planes of a rotating triaxial galaxy with a central core. They found three prograde sequences of stable orbits in addition to the retrograde sequences. Inside the core of the galaxy, they found that the  $x$ -axial orbit was stable and generated a family of box orbits that underwent “envelope doubling” as they looped around the center due to the Coriolis forces.

The first attempt to construct a self-consistent triaxial galaxy with slow figure rotation was presented in the pioneering work of Schwarzschild (1982). Based on previous studies of periodic orbits, Schwarzschild restricted his rotating triaxial models to a moderate pattern speed ( $T_p \sim 1.2 \times 10^9$  yr) for which the main resonances (corotation, outer inner Lindblad, and the Binney instability strip) lay outside the model. He

showed that self-consistent triaxial models with figure rotation could be constructed such that they had either no streaming motions or maximal streaming.

The main conclusion from the early work on figure rotation in triaxial galaxies with cores was that except for the Binney instability associated with retrograde orbits confined to the equatorial plane, several stable sequences of orbits that parented the major orbit families existed over a range of pattern speeds and energies, implying that triaxial galaxies with both fast (rotation period  $T_p \sim 10^6$  yr) and moderate rotation speeds ( $T_p \sim 10^9$  yr) could exist. Our findings here will show that the presence of a central cusp or SMBH alters that conclusion.

Gerhard & Binney (1985) first proposed that the box orbits which form the back bone of triaxial elliptical galaxies would become chaotic due to scattering by the divergent central force arising from a central black hole. The presence of a significant fraction of chaotic orbits results in chaotic mixing which can cause secular relaxation of orbits in phase space (Kandrup & Mahon 1994) resulting in a change in the shape of the galaxy from triaxial to axisymmetric on timescales of order  $\sim 30$ -50 dynamical times (Merritt & Valluri 1996; Merritt & Quinlan 1998). Gerhard & Binney (1985) had also argued, however, that if the triaxial potential had figure rotation, then box orbits (which are crucial to maintaining triaxiality) would be less affected by the central force in the rotating frame due to “envelope doubling” (de Zeeuw & Merritt 1983).

Several early studies indicated that triaxial galaxies with figure rotation could often have significant fractions of chaotic orbits. The studies by (Udry & Pfenniger 1988; Martinet & Udry 1990; Udry 1991; Tsuchiya et al. 1993) were however restricted to limited numbers of orbits in models with cores and did not pursue the primary cause of this chaos.

It is now believed that all elliptical galaxies have either shallow or steep central density cusps (Gebhardt et al. 1996; Lauer et al. 2007) and central SMBHs (Ferrarese & Merritt 2000; Gebhardt et al. 2000). In realistic elliptical galaxy models with cusps and black holes, a large fraction of phase space is occupied by resonant and chaotic orbits (Miralda-Escude & Schwarzschild 1989; Schwarzschild 1993; Valluri & Merritt 1998; Merritt & Valluri 1999; Poon & Merritt 2004). Although the fraction of chaotic orbits increases with an increase in the strength of the density cusp (Schwarzschild 1993; Merritt & Fridman 1996; Merritt 1997) or the mass of the central black hole (Merritt & Valluri 1996), it is still possible to construct triaxial models that do not evolve rapidly due to chaotic mixing so long as a significant fraction of orbits ( $\sim 50\%$ ) are regular (Poon & Merritt 2002, 2004).

In a precursor to the present paper, Valluri (1999) first showed that box orbits in triaxial galaxies with cusps and black holes are destabilized by moderate amounts of figure rotation because the envelope doubling acts to further destabilize the resonant box orbits, rather than stabilize chaotic orbits as predicted by Gerhard & Binney (1985). This paper further explores the cause of the destabilization of box-like orbits and investigates the effects of figure rotation on all major orbit families.

Our objective in this paper is to study the behavior of all the major and minor orbit families, especially those that form the backbone of realistic rotating triaxial galaxy models. The goal is to identify the range of rotation speeds for which such orbits will remain stable.

The paper is organized as follows. In Section 2, we describe

the numerical model, the selection of orbital initial conditions, and the Laskar mapping method (Laskar 1990). In Section 3, we describe the results of our analysis of the effects of figure rotation on major orbit families, as a function of pattern speed, orbital energy, and the shape of the triaxial model, in models with and without central SMBHs. We summarize our results and discuss the implications of our findings in Section 4.

## 2. MODELS AND NUMERICAL METHODS

### 2.1. Density model

We studied triaxial generalizations of spherical models first presented by Dehnen (1993) and Tremaine et al. (1994). The model, which we will henceforth refer to as the “Dehnen-model”, has a density law that is a good fit to the observed luminosity profiles of ellipticals and the bulges of spirals, and is given by

$$\rho(m) = \frac{(3-\gamma)M}{4\pi abc} m^{-\gamma}(1+m)^{-(4-\gamma)}, \quad 0 \leq \gamma < 3, \quad (1)$$

where

$$m^2 = \frac{x^2}{a^2} + \frac{y^2}{b^2} + \frac{z^2}{c^2}, \quad a \geq b \geq c \geq 0, \quad (2)$$

and  $M$  is the total mass of the model. The mass distribution is stratified on concentric ellipsoids where  $a, b$ , and  $c$  are the scale lengths of the semimajor, semi-intermediate, and semiminor axes of the model, which are aligned with Cartesian coordinates  $x, y$ , and  $z$ , respectively. The parameter  $\gamma$  which determines the logarithmic slope of the central density cusp ranges observationally from  $\gamma = 0.5$ -1 in luminous galaxies with “shallow cusps” (sometimes called a “core”) to  $\gamma = 2$  in the lower luminosity galaxies with “steep cusps” (Gebhardt et al. 1996; Lauer et al. 2007). At large radii the density profile of the model always falls as  $m^{-4}$ . The model has a finite density core for  $\gamma = 0$  and an infinite central density for  $\gamma > 0$ . The potential ( $\Phi(\mathbf{x})$ ) and forces in the stationary triaxial Dehnen model in ellipsoidal coordinates are taken from Merritt & Fridman (1996).

In the rotating frame, the energy of an orbit is not an integral of motion but the Jacobi integral ( $E_J$ ) is a conserved quantity:

$$E_J = \frac{1}{2} |\dot{\mathbf{x}}|^2 + \Phi - \frac{1}{2} |\Omega_p \times \mathbf{x}|^2, \quad (3)$$

where  $\mathbf{x}$  and  $\dot{\mathbf{x}}$  are three-dimensional spatial and velocity vectors, respectively.

In our models, figure rotation is about the short ( $z$ ) axis, hence  $\vec{\Omega}_p = \Omega_p \hat{e}_z$  and equations of motion in the rotating frame (BT08, Section 3.3.2) become

$$\ddot{\mathbf{x}} = -\nabla\Phi - 2(\vec{\Omega}_p \times \dot{\mathbf{x}}) - \vec{\Omega}_p \times (\vec{\Omega}_p \times \mathbf{x}) \quad (4)$$

$$= -\nabla\Phi - 2(\vec{\Omega}_p \times \dot{\mathbf{x}}) + |\Omega_p|^2 \mathbf{x}. \quad (5)$$

In Cartesian coordinates the equations of motion are then given by

$$\ddot{x} = -\frac{\partial\Phi}{\partial x} - 2\Omega_p y + \Omega_p^2 x, \quad (6)$$

$$\ddot{y} = -\frac{\partial\Phi}{\partial y} + 2\Omega_p x + \Omega_p^2 y, \quad (7)$$

$$\ddot{z} = -\frac{\partial\Phi}{\partial z}, \quad (8)$$

where  $-2\Omega_p y$  and  $2\Omega_p x$  are Coriolis force terms and  $\Omega_p^2 x$  and  $\Omega_p^2 y$  are centrifugal force terms.<sup>4</sup>

Most of the models used in this study are close to maximally triaxial with triaxiality parameter  $T = (a^2 - b^2)/(a^2 - c^2) = 0.58$  and minor to major axis ratio  $c/a = 0.5$ . For a limited number of models, we also explored the effect of changing the shape of the triaxial figure with  $c/a = 0.5, 0.8$ , and  $0.7$  with triaxiality parameters  $T = 0.1, 0.9$ , and  $0.3$ , respectively. The shapes therefore range from nearly oblate, through oblate triaxial to nearly prolate.

Following the standard practice, we adopt a set of units where the total galactic mass  $M$ , the semimajor axis scale length  $a$ , and the gravitational constant  $G$  are set to unity. When a central black hole is added to the model, its mass  $M_{bh}$  is expressed as a fraction of the total galaxy mass  $M$ . In this paper we restrict ourselves to studying models with either no central point mass ( $M_{bh} = 0$ ) or models with  $M_{bh} = 0.001$  (i.e., 0.1% of the mass of the galaxy). The latter value is consistent with  $0.14\% \pm 0.04\%$  the mass fraction in a central SMBH that is expected to be found in most elliptical galaxies (Häring & Rix 2004). The potential and forces due to the central black hole are those of a softened point mass with softening length  $\epsilon = 10^{-5}a$ .

The orbital structure of the stationary versions of triaxial Dehnen models with various cusp slopes and a range of black hole mass fractions have been previously studied (Merritt & Fridman 1996; Valluri & Merritt 1998; Siopis & Kandrup 2000). In this paper we restrict ourselves to presenting models with  $\gamma = 1$  for the following reasons. First, the most likely candidates for triaxial elliptical galaxies with slow figure rotation are the more luminous “slow rotators” with shallow central cusps (Emsellem et al. 2007). Second, a Dehnen model with  $\gamma = 1$  is quite similar (at least in the inner regions) to the density profiles of cosmological dark matter halos with the main difference being that cosmological density profiles fall off more slowly at large radii ( $r^{-3}$  compared to  $r^{-4}$  for the Dehnen model). Models with  $\gamma = 2$  were studied (but are not presented) since their dependence on pattern speed is qualitatively similar to that of the  $\gamma = 1$  models with an SMBH. (We note that while our choice of triaxial potential is representative of a triaxial elliptical galaxy, it is an incomplete representation of a dark matter halo which could have a significant potential contribution from a stellar disk.)

At the present time only a few measurements of the pattern speeds of figure rotation in triaxial dark matter halos and early-type galaxies exist. The pattern speeds of fast bars measured by applying the Tremaine–Weinberg method (Tremaine & Weinberg 1984; Meidt et al. 2008) typically indicate that the ratio of the corotation radius to the length of the bar  $R_\Omega/a = [1, 1.4]$  (for a bar of semi-major axis length  $a$ ) (e.g., Debattista et al. 2002; Aguerri et al. 2003; Corsini 2010; Binney & Tremaine 2008). Hereafter we shall use the quantity  $R_\Omega/a_i$  to compare the pattern speeds of orbits launched from different radial shells (of semimajor axis length  $a_i$ ) to each other and to the pattern speeds of bars.

The pattern speed of early-type galaxy NGC 2974 has been measured by fitting the properties of three rings of recent star formation (Jeong et al. 2007). This galaxy is normally clas-

<sup>4</sup> Following current convention (e.g., BT08) we use the right-handed screw rule (with positive angular momentum vector pointed up) for figure rotation and a right-handed coordinate system. Note that some previous authors (Schwarzschild 1982) used a left-handed screw rule for figure rotation and a right-handed coordinate system.

sified as E4, but the authors argue that all three rings can be accounted for as occurring at resonances if this galaxy is a S0 galaxy with an extended stellar bar and pattern speed,  $\Omega_p \sim 78 \pm 6 \text{ km s}^{-1} \text{ kpc}^{-1}$ . This pattern speed is only slightly slower than that of fast bars. Figure rotation of a triaxial dark matter halo was proposed as the cause of the extended spiral arms in the blue compact dwarf galaxy NGC 2915 (Bureau et al. 1999; Bekki & Freeman 2002) whose modeling required a halo pattern speed of  $\Omega_p = 7 \pm 1 \text{ km s}^{-1} \text{ kpc}^{-1}$ . This pattern speed is an order of magnitude larger than the maximum pattern speed measured for dark matter halos produced in cosmological  $N$ -body simulations ( $\Omega_p = 1.01h \text{ km s}^{-1} \text{ kpc}^{-1}$ ) and nearly two orders of magnitude larger than the median pattern speed ( $\Omega_p = 0.148h \text{ km s}^{-1} \text{ kpc}^{-1}$ ) (Bailin & Steinmetz 2004). Thus, at the present time, observational constraints on the pattern speeds of triaxial halos and elliptical galaxies are quite uncertain. Our fastest pattern speed  $\Omega_p = 34 \text{ km s}^{-1} \text{ kpc}^{-1}$  (for  $R_\Omega/a = 2$ ) is slightly slower than the speeds observed in fast bars, our slowest  $\Omega_p = 0.58 \text{ km s}^{-1} \text{ kpc}^{-1}$  (for  $R_\Omega/a = 40$ ) is comparable to fastest measured in simulations of dark matter halos. We explore a range of values for  $\Omega_p$  between these limits.

The triaxial Dehnen models studied here rotate about the short axis ( $z$ ). Simulations of collisionless dark matter halos show that the angular momentum axes have a mean misalignment of  $\sim 25^\circ$  with the minor axis (Bailin & Steinmetz 2005). However, the dissipative collapse accompanying galaxy formation is likely to induce angular momentum transport and a higher degree of alignment between the spin axis and the short axis of the galaxy. The pattern speed of the triaxial figure is given in terms of the ‘‘corotation radius’’, hereafter  $R_\Omega$ . In a nearly axisymmetric potential, the corotation radius is the radius at which the frequency  $\Omega_c$  of a closed (almost circular) orbit in the equatorial ( $x$ - $y$ ) plane of the potential is the same as the pattern frequency (generally called ‘‘pattern speed’’)  $\Omega_p$ :

$$\Omega_p = \Omega_c = \left[ \sqrt{\frac{1}{R} \nabla \Phi} \right]_{R=R_\Omega, z=0}. \quad (9)$$

Working in the equatorial plane of our triaxial model we set  $R^2 = (x/a)^2 + (y/b)^2$ . In our models  $R_\Omega$  is given in units of  $a$ , the scale length of the semimajor axis, and ranges from  $R_\Omega = 60$  (slowly rotating) to  $R_\Omega = 2$  (very rapidly rotating) (see Table 1). In this nomenclature the stationary (non-rotating) model has its corotation radius at infinity and is labeled with  $R_\Omega = \infty$ . We do not discuss the orbital structure of more prolate triaxial structures similar to fast bars with higher pattern frequencies ( $R_\Omega \leq 2$ ) since they have been previously studied (Skokos et al. 2002a,b; Harsoula & Kalapotharakos 2009). To give the reader a better physical appreciation of the pattern frequencies implied by the co-rotation radii, we convert our model units to physical units in an elliptical galaxy. For a semi-major axis scale radius  $a = 5 \text{ kpc}$  and a galaxy mass of  $M = 5 \times 10^{11} M_\odot$ , the unit of time for the model is given by

$$T = \sqrt{\frac{a^3}{GM}} = 1.49 \times 10^6 \left[ \frac{a}{\text{kpc}} \right]^{3/2} \left[ \frac{M}{10^{11} M_\odot} \right]^{-1/2} \text{ yr}. \quad (10)$$

For these parameters Table 1 gives the pattern frequency ( $\Omega_p$ ) and rotation period  $T_p = 2\pi/\Omega_p$  (in years) for each value of corotation radius  $R_\Omega$  that was studied.

## 2.2. Orbit start spaces

TABLE 1  
PATTERN FREQUENCIES OF FIGURE ROTATION OF TRIAXIAL DEHNEN  
MODELS WITH  $\gamma = 1$ ,  $M_{bh} = 0$

$R_\Omega$ (a)	$\Omega_p$ (program units)	$\Omega_p^*$ ( $\text{km s}^{-1} \text{ kpc}^{-1}$ )	$T_p^*$ (yrs)
2	$2.57 \times 10^{-1}$	33.8	$1.82 \times 10^8$
5	$7.45 \times 10^{-2}$	9.80	$6.28 \times 10^8$
10	$2.87 \times 10^{-2}$	3.78	$1.63 \times 10^9$
20	$1.09 \times 10^{-2}$	1.44	$4.29 \times 10^9$
40	$3.85 \times 10^{-3}$	0.51	$1.21 \times 10^{10}$
60	$2.12 \times 10^{-3}$	0.28	$2.21 \times 10^{10}$
$\infty$	0.0	0.0	$\infty$

\* For  $a = 5 \text{ kpc}$ ,  $M = 5 \times 10^{11} M_\odot$

Following Merritt & Fridman (1996), the model’s mass distribution is stratified into 20 ellipsoidal shells dividing the model into 21 sections of equal mass. In this paper, we focus mostly on orbits with energy equal to the potential energy at the point the 8th shell intersects the major axis of the model ( $x = 1.6a$ ). (Note that shell 10 corresponds to the half-mass radius of the model). In the rotating potential, orbits were launched from the equi-effective-potential surface which is analogous to launching all orbits in a non-rotating model from an equipotential surface. Thus all orbits launched from a given shell have the same Jacobi integral ( $E_J = E - \frac{1}{2} |\Omega_p \times \mathbf{r}|^2$ ), where  $E$  is the total energy of an orbit. We study orbits on 6 energy shells for one pattern frequency but defer a full investigation of orbits in self-consistent potentials to a future paper (Valluri 2011).

Initial conditions for the orbits were selected in two different ways such that orbits from all four major families (the box orbits and three families of tube orbits) were represented (de Zeeuw 1985). Although models are rotating, the orbits were launched, integrated, examined, and classified only in the frame that is corotating with the figure, allowing for a more direct comparison with the stationary models that have been studied in the past.

In a stationary potential, box orbits are characterized by a stationary point on the equipotential surface. In a rotating potential there are no true box orbits (i.e., orbits with stationary points in an inertial frame). However, orbits that are characterized by a stationary point on the effective potential surface (surface of constant Jacobi integral) look and behave much like box orbits in the frame that is corotating with the figure. Accordingly, we launch orbits at zero velocity on a regular grid on one octant of the effective potential surface to obtain box-like orbits. In a non-rotating triaxial model, a tube orbit is characterized by a finite angular momentum (about either the long or short axis) which oscillates between two values of the same sign. Thus the magnitude of the angular momentum is not a conserved quantity, but the sign of the angular momentum of a tube orbit remains constant<sup>5</sup>. Consequently, tube orbits avoid the center.

For exploring the phase space structure of a stationary triaxial model it is customary (Schwarzschild 1993; Merritt & Fridman 1996; van den Bosch et al. 2008) to launch orbits uniformly from the ‘‘ $x$ - $z$  start space’’ i.e., from one quadrant of the  $x$ - $z$  plane with  $v_x = v_z = 0$  with  $v_y > 0$  determined by the

<sup>5</sup> We refer to tube orbits as ‘‘anti-clockwise’’ or ‘‘clockwise’’ depending on whether their time average angular momentum vector ( $J_x$  for  $x$ -tubes and  $J_z$  for  $z$ -tubes) is positive or negative, respectively (in a right-handed coordinate system)

energy of the equipotential surface, this is adequate for stationary models since the properties of orbits with  $v_y < 0$  are simply obtained by relying on the symmetries of the model. However, in a triaxial model with figure rotation about the short axis, orbits that are launched with  $v_y > 0$  in the  $x$ - $z$  start space are different from those with  $v_y < 0$ . Since orbits of all major families intersect the intermediate  $y$ -axis we use instead the “ $Y$ - $\alpha$  start space” (Schwarzschild 1982) where all four families of orbits are launched from the  $y$ -axis of the model with  $v_y = 0$  and at an angle  $\alpha$  between the starting velocity vector (perpendicular to the  $y$ -axis) and the  $x$ - $y$  plane. The initial conditions for an orbit are given by

$$\begin{aligned} x &= 0 & y &= Y & z &= 0 \\ v_x &= V \cos \alpha & v_y &= 0 & v_z &= V \sin \alpha, \end{aligned}$$

where  $V$  is the magnitude of the total velocity of the orbit at that position determined from potential energy at the starting point and the Jacobi integral of all orbits on that surface. By allowing  $0^\circ \leq \alpha \leq 360^\circ$  we obtain tube orbits with both clockwise and anti-clockwise motions. Figure 1 shows the  $Y$ - $\alpha$  start space with 225 different initial conditions marked by their orbital types. (We plot  $-30 < \alpha < 330$  to illustrate that the retrograde  $z$ -tubes wrap around the top and bottom boundaries.) The maximum value of  $Y$  is determined by the intersection of the equipotential surface with the  $y$ -axis.

The orbital types were determined visually by plotting three different projections in coordinate space ( $x$ - $y$ ,  $y$ - $z$ , and  $x$ - $z$ ) and by examining their time-averaged normalized angular momenta about the three principal axes (i.e.,  $\langle J_x/|J_x| \rangle$ ,  $\langle J_y/|J_y| \rangle$ , and  $\langle J_z/|J_z| \rangle$ ). For a box orbit (or strongly chaotic orbit), all three components of normalized angular momentum are approximately zero. For  $x$ -axis tubes and  $z$ -axis tubes, the absolute values of the  $x$  and  $z$  components are equal to unity (within 0.005%). Note that a weakly chaotic orbit associated with a tube family will have  $\langle J_x/|J_x| \rangle \sim 1$  or  $\langle J_z/|J_z| \rangle \sim 1$  over a finite number of orbital periods. In a three dimensional potential, Arnold diffusion would cause such an orbit to eventually ergodically fill the entire energy surface available to it and would therefore not be identifiable as a tube orbit (Lichtenberg & Lieberman 1992). Hereafter, we refer to such orbits as “tube-like”. Note that this criterion for classifying orbits into three major families relies purely on the relative magnitudes of the three components of the time-averaged angular momenta but does not indicate that these orbits are regular.

Figure 1 shows how orbits of different types are distributed on the  $Y$ - $\alpha$  start space. Squares indicate box orbits, diamonds indicate inner long-axis tubes, triangles indicate outer long-axis tubes, plus signs indicate short-axis tubes while an asterisk indicates an orbit identified as stochastic by its high diffusion rate (see Section 2.3). Note that since the triaxial figure rotates in the anti-clockwise direction about the  $z$ -axis, we refer to anti-clockwise  $z$ -tubes as “prograde” and their clockwise counterparts as “retrograde” (even when a specific model is stationary). We will see in Figure 3 that stochastic orbits are frequently found along the boundaries (or separatrix layers) between regions occupied by different orbit families. The general location of the different regular orbit families in this start space will remain roughly the same as the potential is perturbed with non-zero cusp slope  $\gamma$ , the addition of a central point mass, or as the pattern frequency, orbital energy, or the shape of the figure are altered.

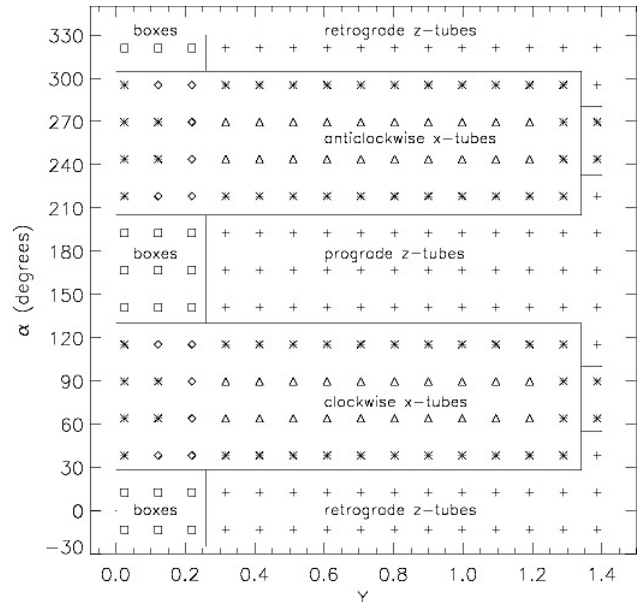


FIG. 1.— Location of different orbit families on the  $Y$ - $\alpha$  start space in a stationary triaxial Dehnen model with  $c/a=0.5$ ,  $T=0.58$ ,  $\gamma=0$ , and  $M_{bh}=0$ . The lines mark approximate boundaries between major families. Squares ( $\square$ ) denote box orbits, asterisks ( $*$ ) denote chaotic orbits, diamonds ( $\diamond$ ) indicate inner long-axis ( $x$ ) tubes, triangles ( $\triangle$ ) denote outer long-axis tubes, and plus signs (+) indicate  $z$ -tubes.

### 2.3. Numerical Analysis of Orbital Frequencies

In fully integrable potentials like the Stäckel potentials, all orbits are confined to  $N$ -dimensional tori, with  $N$  the number of degrees of freedom (dof), i.e., the number of spatial dimensions. Motion on the torus is defined in terms of the fundamental frequencies  $\omega_i$ ,  $i = 1, \dots, N$ , the rates of change of the corresponding angle variables. Expressed in terms of Cartesian coordinates, the motion is quasi-periodic, e.g.,

$$x(t) = \sum_{k=1}^{\infty} A_k e^{i\nu_k t}, \quad (11)$$

where the  $\nu_k$ 's are linear combinations, with integer coefficients, of the three fundamental frequencies:

$$\nu_k = n_{1,k}\omega_1 + n_{2,k}\omega_2 + n_{3,k}\omega_3 \quad (12)$$

and the  $A_k$  are the corresponding amplitudes. The same is true for regular orbits in arbitrary potentials, i.e., for orbits that respect at least three isolating integrals of the motion (e.g., Lichtenberg & Lieberman 1992).

When a regular orbit is followed for many ( $\sim 100$ ) dynamical times, a Fourier transform of the trajectory yields a spectrum with discrete peaks. The locations of the peaks in the spectrum correspond to the frequencies  $\nu_k$  in Equation (11) and can be used to compute the three fundamental frequencies and the integer coefficients ( $n_{1,k}, n_{2,k}, n_{3,k}$ ) that correspond to each peak (e.g., Binney & Spergel 1982).

Laskar (1990) developed a fast and accurate numerical technique (“Numerical Analysis of Fundamental Frequencies,” hereafter NAFF) to decompose a complex time series representation of the phase space trajectory of the form  $x(t) + iv_x(t)$ . Our own implementation of Laskar’s algorithm uses integer programming to obtain the fundamental frequencies from the spectrum (Valluri & Merritt 1998, hereafter VM98). We integrated orbits using an explicit Runge Kutta

integrator (DOP853) of order eight (5,3) due to Dormand & Prince with stepsize control and dense output by Harier and Wanner (Harier et al. 1993). The orbit integration, orbit classification, and frequency analysis were all carried out in the frame that is corotating with the pattern frequency of the figure.

Even for regular orbits, the character of the motion depends critically on whether the three fundamental frequencies are independent or whether they satisfy one or more nontrivial linear relations of the form

$$\ell\omega_1 + m\omega_2 + n\omega_3 = 0 \quad (13)$$

where  $(\ell, m, n)$  are integers, not all of which are zero. Generally there exists no relation like Equation (13); the frequencies are incommensurable, and the trajectory fills its torus uniformly and densely in a time-averaged sense. When one or more resonance relations are satisfied, however, the trajectory is restricted to a phase space region of lower dimensionality than  $N$ .

In 2 dof systems, a resonance implies a closed, or periodic, orbit, e.g., a “boxlet” (Miralda-Escude & Schwarzschild 1989). In three dimensions, a single resonance relation like Equation (13) does not imply that an orbit will be closed; rather, it restricts the orbit to a space of dimension two (Merritt & Valluri 1999). An orbit satisfying one such relation is “thin,” confined for all time to a (possibly self-intersecting) membrane. In order for an orbit in a 3 dof system to be closed, it must satisfy two such independent relations; such orbits are likely to be much rarer than thin orbits. In what follows, we will use the term “resonant” to refer both to thin orbits (satisfying one relation like Equation 13) and to closed orbits (satisfying two such relations), e.g., boxlets. Stable resonances of both sorts generate new families of regular orbits whose shape mimics that of the parent orbit. Unstable resonant tori are typically associated with a breakdown of integrability and with chaos.

Once the fundamental frequencies and their amplitudes are obtained, it is possible to obtain two complementary representations of phase space at a given energy. A *frequency map* is obtained by plotting ratios of pairs of frequencies (e.g.,  $\omega_x/\omega_z$  versus  $\omega_y/\omega_z$ ) for many thousands of orbits in the potential. Such a representation of phase space (e.g., Figure 3(a) and Figure 2(a)) is particularly useful for identifying the most important orbital resonances. Stable resonances appear as filled lines with an increased density of orbits clustered along them. This is because these orbits have been trapped by the stable resonance. In contrast, unstable resonances appear as “blank” or depopulated lines and are associated with stochastic orbits.

Laskar (1990) demonstrated that since most orbits in realistic galactic potentials are only weakly chaotic, they lie close to regular orbits in phase space mimicking their regular behavior over finite time intervals. Consequently, frequency analysis can be used to distinguish between regular and chaotic orbits. The frequency drift can give a measure of the degree of chaos in an orbit. The frequency drift of an orbit can be determined from the change in its fundamental frequencies measured over two consecutive time intervals.

In applying Laskar’s formalism, we integrated each orbit for  $100T_D$ , where  $T_D$  is the period of the long-axis orbit of the same energy in the stationary model. The time interval was divided into two equal segments labeled  $t_1$  and  $t_2$  and three fundamental frequencies  $\omega_x(t_1), \omega_y(t_1), \omega_z(t_1)$  and  $\omega_x(t_2), \omega_y(t_2), \omega_z(t_2)$  were computed in each time segment. The “frequency drift” or “diffusion parameter” in each frequency

component is given by

$$\log(\Delta f_x) = \log \left| \frac{\omega_x(t_1) - \omega_x(t_2)}{\omega_x(t_1)} \right|, \quad (14a)$$

$$\log(\Delta f_y) = \log \left| \frac{\omega_y(t_1) - \omega_y(t_2)}{\omega_y(t_1)} \right|, \quad (14b)$$

$$\log(\Delta f_z) = \log \left| \frac{\omega_z(t_1) - \omega_z(t_2)}{\omega_z(t_1)} \right|. \quad (14c)$$

We define the diffusion parameter  $\log(\Delta f)$  to be the value associated with the largest of the three amplitudes  $A_x, A_y$ , and  $A_z$ . The larger the value of the diffusion parameter the more chaotic the orbit. Our second representation of phase space, a *diffusion map*, is obtained by plotting the initial conditions of many thousands of orbits and adding a gray scale (or color intensity scale) corresponding to the diffusion parameter. In a diffusion map (e.g., Figure 2(b) and Figure 3(b)) the gray scale (or intensity of the color) corresponds to  $\log(\Delta f)$  such that regions of initial condition space occupied by regular orbits are white and those occupied by chaotic orbits are dark.

Several properties of the phase space can be inferred from frequency and diffusion maps. We begin with a discussion of phase space maps for the stationary (here after “box orbit”) start space for a baseline model, namely a triaxial Dehnen model with  $c/a = 0.5, T = 0.58, \gamma = 0$ , and  $M_{bh} = 0$ . The frequency map in Figure 2(a) shows a plot of the ratios of fundamental frequencies  $\omega_x/\omega_z$  versus  $\omega_y/\omega_z$  for each of 9408 box orbits dropped with zero velocity from the equipotential surface corresponding to the 8th shell.

Note that although we focus primarily on the behavior of orbits launched from shell 8th, the behavior of an orbit in response to figure rotation depends both on the (radial) energy shell from which it is launched as well as the co-rotation radius. However, since the density profile has an approximately power-law profile outside the inner cusp, the behavior of orbits depends primarily on  $R_\Omega/a_i$ , where  $a_i$  is the semi-major axis of the  $i$ th shell. Consequently, the behavior of orbits launched from an outer shell at a moderate pattern speed can resemble that of orbits launched at an inner radius and a faster pattern speed. Consequently, we will frequently give values of  $R_\Omega/a_i$  as well as  $R_\Omega$ .

The frequency map shows that most points at the bottom left corner of the plot lie on a fairly regular grid which reflects the regular distribution of initial conditions. Away from this region the regular, grid-like structure is disrupted by the appearance of dark lines corresponding to stable resonances and their associated regular orbits. All the orbits lying along such lines obey a single resonant condition like that of Equation (13). In the plot, several such resonances are highlighted with dashed lines and are labeled with their defining integers  $(\ell, m, \text{ and } n)$ .

Figure 3(a) shows a frequency map for 10,000 orbits initialized on the  $Y - \alpha$  start space with the energy corresponding to the  $x$ -axial orbit on shell 8 in this model. In this frequency map, all four major orbit families are represented: box orbits are black, anti-clockwise  $x$ -tubes are blue, clockwise  $x$ -tubes are cyan, clockwise  $z$ -tubes are ochre, and anti-clockwise  $z$ -tubes are red. Note that a significant fraction of the  $z$ -tubes (red and ochre points) and  $x$ -tubes (blue and cyan points) appear clustered along straight lines. These are orbits that lie close to the thin-shell tube orbit parent of the family and appear as “resonance lines” in the frequency map although they are not traditionally viewed as resonances. To accurately rep-



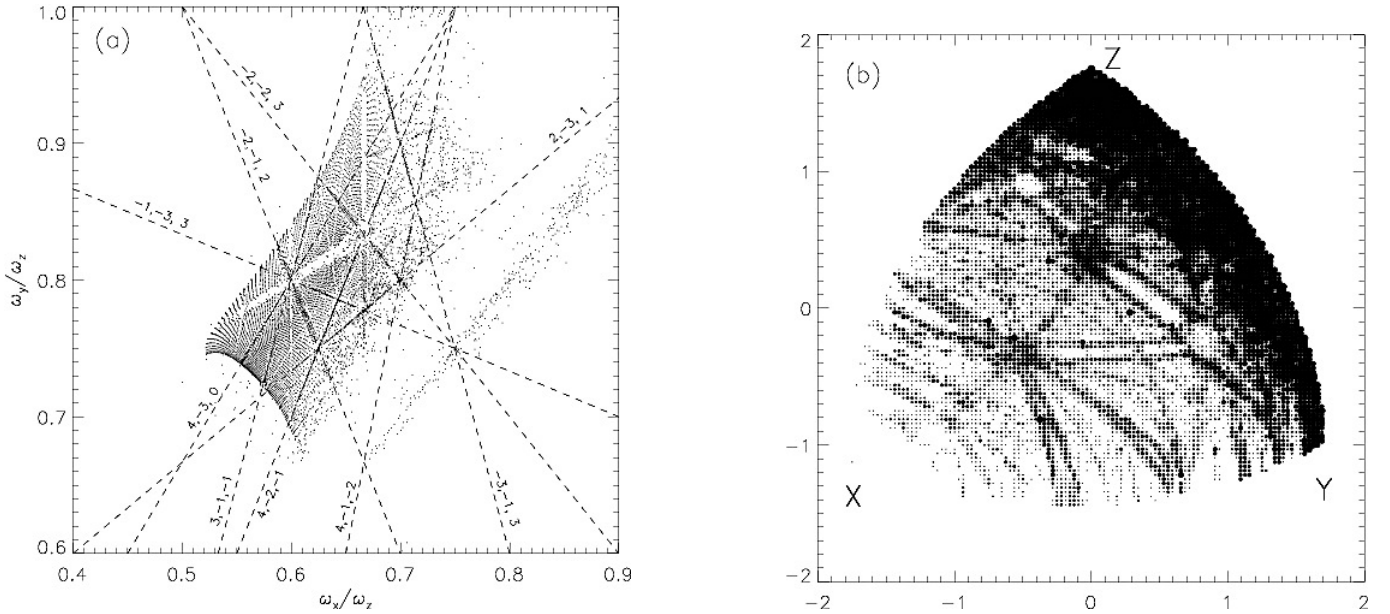


FIG. 2.— Two representations of phase space for 9408 box orbits launched from shell 8 in a non-rotating triaxial Dehnen model ( $c/a = 0.5$ ,  $T = 0.58$ ,  $\gamma = 0$ , and  $M_{bh} = 0$ ). (a) A frequency map:  $\omega_x/\omega_z$  versus  $\omega_y/\omega_z$  for the fundamental frequencies given by the NAFB algorithm. Dashed lines mark various important resonances labeled by their integers ( $\ell, m$ , and  $n$ ). (b) Diffusion map: gray scale corresponds to the diffusion parameter ( $\log(\Delta f)$ ) of orbits at various initial positions on one octant of the equipotential surface (the “stationary (box orbit) start space”). Dark regions on the map correspond to chaotic orbits and white regions correspond to regular orbits. The labels “X”, “Y”, and “Z” mark the intersections of the equipotential surface with the three principal axes.

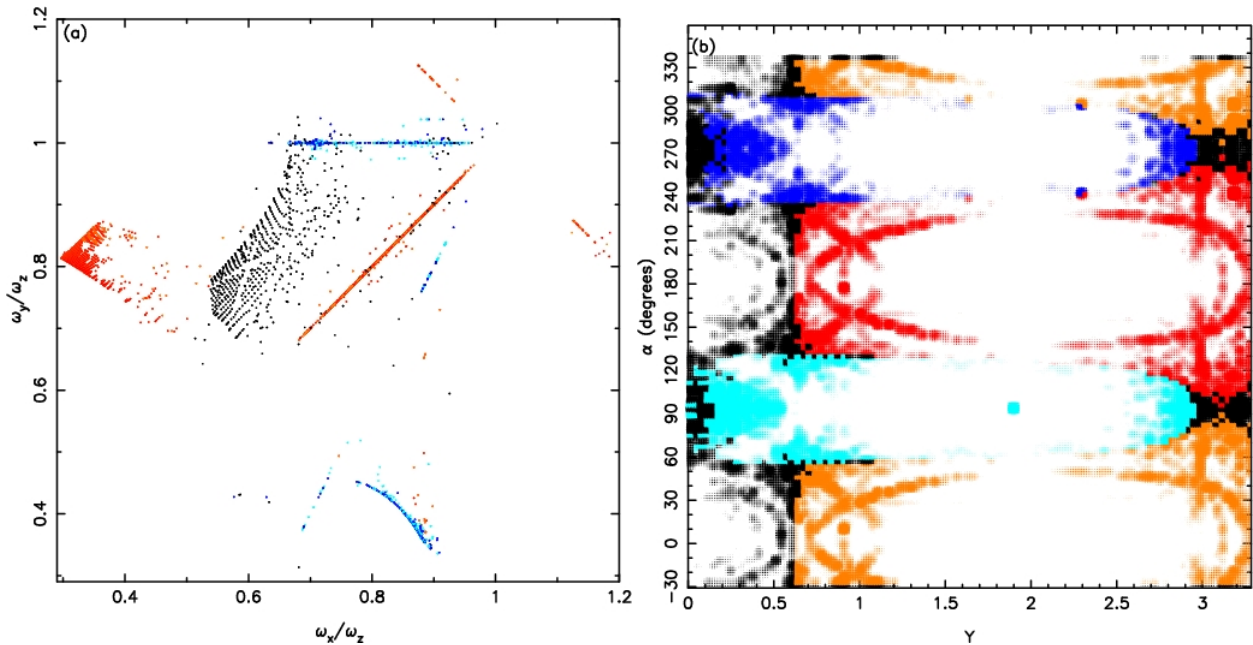


FIG. 3.— (a) Frequency map and (b) diffusion map for 10,000 orbits in the “ $Y$ - $\alpha$  start space” for a model with  $c/a = 0.5$ ,  $T = 0.5$ , and  $\gamma = 0$ . Orbit families are color coded so that box orbits are black, anti-clockwise  $x$ -tubes are blue, clockwise  $x$ -tubes are cyan, clockwise (retrograde)  $z$ -tubes are ochre, and anti-clockwise (prograde)  $z$ -tubes are red. In the diffusion map only the chaotic orbits appear colored since the intensity of the color depends on the orbital diffusion parameter.

represent the resonances in the two tube orbit families it is essential to obtain the fundamental frequencies in cylindrical coordinates about the appropriate symmetry axis. VM98 showed that such a representation reveals several unstable tube orbit resonances. These can be seen as dark bands in Figure 3(b).

Figure 2(b) is a diffusion map for 9408 box orbits launched with zero initial velocity from the equipotential surface (at shell 8) of a stationary maximally triaxial Dehnen model with  $\gamma = 0$ . The large swath of regular orbits at the bottom left

of the diffusion plot consists of regular box orbits that originate close to the  $x$ -axis. In addition, several white bands mark regular islands of resonant boxlet families. Each white band corresponds to a dark resonance line in the frequency map in Figure 2(a). Most white bands are flanked by narrow dark regions (occupied by stochastic orbits) which lie along the “separatrix” (transition layer) between different orbit families. Stochastic orbits (dark regions) are also seen at the intersections of stable resonances (white bands), when the parent pe-

riodic orbit is unstable. The prominent dark band of chaotic orbits that runs along the right edge of the diffusion map corresponds to orbits originating close to the  $y$ - $z$  plane. Orbits in this region are chaotic due to the well-known instabilities of the  $y$ -axial and  $z$ -axial orbits (Heiligman & Schwarzschild 1979; Heisler et al. 1982; de Zeeuw & Merritt 1983; Adams et al. 2007) as well as due to the instability of orbits confined in the  $y$ - $z$  plane to perturbations perpendicular to this plane (Adams et al. 2007). This region will be seen to expand with increasing figure rotation and is referred to hereafter as the “ $y$ - $z$  instability band”. Most of these features were described in detail in previous papers (Valluri & Merritt 1998; Merritt & Valluri 1999).

Figure 3(b) shows a diffusion map for 10,000 orbits launched from the  $Y$ - $\alpha$  start space. The orbits were classified into three different orbit families based on their time-averaged normalized angular momentum values. The boxes are colored black, anti-clockwise  $x$ -tubes are blue, clockwise  $x$ -tubes are cyan, clockwise (retrograde)  $z$ -tubes are ochre, and anti-clockwise (prograde)  $z$ -tubes are red. Note that regions of more intense color (occupied by stochastic orbits) generally appear at the separatrix between the major orbit families. Within the regions occupied by  $x$ -axis tubes (blue and cyan regions), the transition between the inner and outer  $x$ -axis tubes is also marked by a weakly stochastic layer. Thick stochastic layers separate the  $z$ -tubes from the box orbits that lie at values of  $Y < 0.5$ . In addition, stochastic orbits are found at  $\alpha \sim 90^\circ \pm 30^\circ$  and  $\alpha \sim 270^\circ \pm 30^\circ$  mostly at very small  $Y$  values (these orbits are launched nearly along the  $z$  axis which is known to be unstable).

The main features identified on the frequency and diffusion maps above, for the  $\gamma = 0$  and  $M_{bh} = 0$  case, are meant to give readers insight into how they should interpret the results for models with figure rotation.

### 3. RESULTS

We now discuss the effects of increasing the pattern frequency of figure rotation on box-like and tube-like orbits using the phase-space mapping techniques discussed in the previous section.

#### 3.1. Effects of slow/Moderate pattern frequency on boxlike orbits

Box orbits were integrated, from start spaces such as the one in Figure 2(b), for various model parameters and increasing pattern speeds. We generally present results for a default model which is close to maximally triaxial, with  $c/a = 0.5$ ,  $T = 0.58$  and central density cusp of  $\gamma = 1$ . We also present results for models with a central point mass representing a central SMBH with  $M_{bh} = 0.001$  (0.1% of the galaxy mass). (Models with  $\gamma = 2$  were studied but are not presented since their dependence on  $R_\Omega$  is qualitatively similar although they have a higher fraction of chaotic orbits, VM98. Higher black hole mass fractions were previously studied by VM98 and were found to induce more chaos.) In each figure, we show phase space maps for a non-rotating model ( $R_\Omega = \infty$ ) and three additional values of the corotation radius ( $R_\Omega = 40, 10$ , and 5). In all cases orbits were launched with energy  $E$  equal to that of the  $x$ -axial orbit started from the 8th shell. Therefore, for an orbit launched from the 8th shell, these pattern speeds correspond to  $R_\Omega/a_i = 24.8, 6.2$ , and 3.1.

Figure 4 shows phase space diffusion maps for box orbits in our default model with no central point mass. The non-rotating model (panel (a)) is similar to (Figure 2(b)) but con-

tains a somewhat larger fraction of stochastic orbits. Almost all the regular orbits (white regions on the map) are now associated with resonant islands containing boxlet families. All orbits that qualitatively resemble box orbits in cored potentials are mildly to strongly chaotic.

As mentioned in Section 1, Gerhard & Binney (1985) first proposed that the box orbits rendered chaotic due to scattering by a massive central point mass could be stabilized in a rotating frame due to the envelope doubling effect of the Coriolis force. Since a box orbit (in a stationary model) has no net angular momentum it oscillates between stationary points reversing its sense of progression around the center each time it reaches a turning point. In a rotating frame this means that the path described during the prograde segment of the orbit is not retraced during the retrograde segment because the Coriolis force on the two segments differs (Schwarzschild 1982; de Zeeuw & Merritt 1983).

We see in Figure 4 that this prediction does not hold up in realistic triaxial galaxy models. In fact, as the pattern frequencies of figure rotation increase ( $R_\Omega$  decreases) the area of the diffusion map occupied by regular orbits (white) decreases and the resonant islands shrink until only a small fraction of orbits remain regular at  $R_\Omega = 5$ . When a central point mass is added, the increase in the fraction of chaotic orbits is even more significant (Figure 5) and in addition the delineation between the various resonant box orbit families is even less clear – pointing to increased resonance overlap. We see from a comparison of the Figures 4 and 5 that high pattern speed increases the fraction of chaotic orbits more significantly than the presence of a central black hole.

We note in passing that a new regular orbit family appears as a white region in the lower right hand corner of the diffusion maps in Figures 4 and 5 for  $R_\Omega = 10, 5$ . In the stationary model, box orbits originating here are highly unstable since they lie close to the unstable  $y$ -axis. Figure 11(top row) shows two projections of one such orbit in a model with  $R_\Omega = 5$ . Although it is launched with no net angular momentum in the rotating frame, this orbit is a short-axis tube. This tube orbit (like others in triaxial potentials) does not conserve angular momentum, but its value oscillates between two values (in this case zero and a large negative value) indicating that its motion in the rotating frame is retrograde to that of the figure. This new family of orbits lies close to the  $x$ - $y$  plane. This family appears to arise when the pattern frequency of the figure is high enough that Coriolis and centrifugal forces cause it to loop around the center. Orbits in this region of start space were chaotic in the stationary model and are indeed stabilized by figure rotation as predicted by Gerhard & Binney (1985). However, this stabilization results from a complete transformation of the orbital character from box-like to tube-like, rather than due to a small deflection of the chaotic box orbit around the destabilizing center. We will see later (Section 3.3) that as the corotation radius moves inward, this region of stable tube-like orbits grows steadily till most of the box start space is occupied by regular orbits, similar to this one.

Figures 4(a) and 5(a) show that most (but not all) the regular orbits in the stationary model, which appear as white regions on the diffusion maps, are associated with resonant orbits. There are two reasons why the majority of box orbits (which are associated with two-dimensional resonance surfaces) are not stabilized by slow to moderate figure rotation as predicted by Gerhard & Binney (1985).

First, the increase in the fraction of chaotic orbits can be



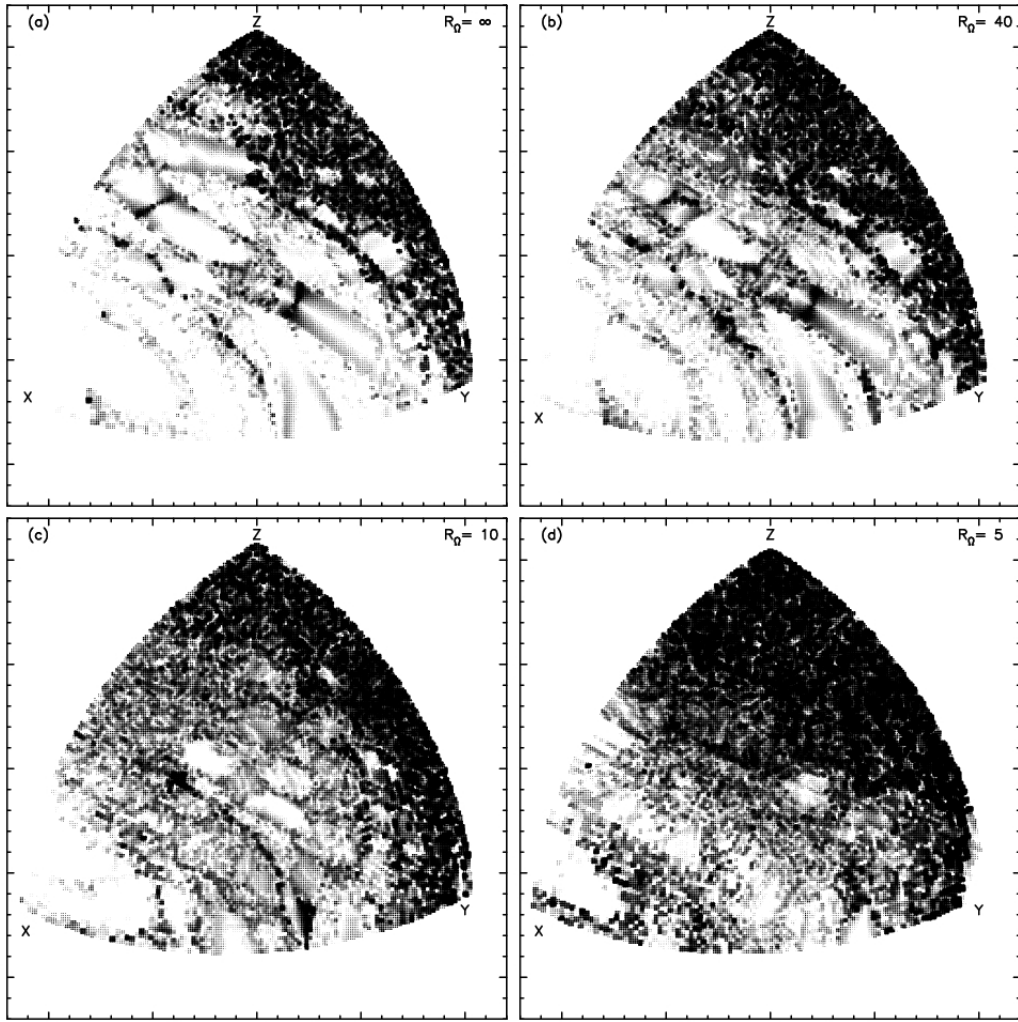


FIG. 4.— Diffusion maps of orbits launched from the box orbit start space at 8th energy shell in models with  $\gamma = 1$  and  $M_{bh} = 0$  and varying pattern frequencies as indicated by labels. The value of  $R_\Omega = \infty$  refers to a model with no rotation, while  $R_\Omega = 40, 10,$  and  $5$  refer to the corotation radii of models with increasing pattern frequencies. These pattern speeds correspond to  $R_\Omega/a_i = 24.8, 6.2,$  and  $3.1$ .

attributed to the distinct configuration space structure of resonant orbits. As described by Merritt & Valluri (1999), the parent of a resonant orbit family satisfies a condition like  $l\omega_x + m\omega_y + n\omega_z = 0$ . This additional resonant condition confines a resonant orbit to the surface of a two-dimensional torus in three-dimensional phase space. In general, such orbits are not periodic. The more commonly known (but less numerous) near-periodic versions of such resonances were identified by Miralda-Escude & Schwarzschild (1989) and given names such as “bananas”, “pretzels”, “fish” etc. based on their projected shapes. A non-periodic resonant orbit therefore, in comparison, appears similar to a three-dimensional box orbit in projection but occupies only a two-dimensional surface in configuration space. Consequently, all families of stable resonant orbits are centrophobic and avoid the center of the potential due to their thin sheet-like structure. The parent of the resonant family is surrounded by a region occupied by nearly resonant orbits which are characterized by two of the same frequencies as the resonant parent, but with an increasing third frequency. As the third frequency increases from zero, the thickness of the orbit increases and the nearest distance of approach to the center of the potential (the pericenter distance) decreases. When the orbit becomes thick enough to pass through the center it is destabilized. The instability at the

center is a consequence of the divergent central density cusp or central black hole present in all realistic galaxy models.

In the rotating frame of a slowly rotating model, the Coriolis force can produce “envelope doubling” which broadens a nearly resonant box orbit driving it into the divergent central cusp (or central black hole), reducing the sizes of stable resonant islands, and eventually destroying them. The effect of envelope doubling can be seen in Figure 6, which shows a resonant boxlet orbit associated with the  $(3, -1, -1)$  resonance. The top row shows two Cartesian projections of the orbit,  $x$ - $y$  (left) and  $x$ - $z$  (right). In projection (top row) the orbit appears similar to three-dimensional box orbits. However, the second row shows intersections of the orbit with the  $x$ - $y$  plane (left) and the  $x$ - $z$  plane (right) shows its perfectly sheet-like structure with a clear “hole” in the center. The next three rows show cross sections of the same orbit in models with  $R_\Omega = 40, 20,$  and  $10$ . When  $R_\Omega = 20$  (4th row) the cross section shows that the Coriolis force broadening has caused it to nearly fill the center in the  $x$ - $z$  projection. When  $R_\Omega = 10$  (5th row) the orbit is thick enough to pass through the center rendering it completely chaotic.

While the majority of the regular orbits on the stationary start space in Figure 4 and Figure 5 are associated with resonances, a few regular box orbits are non-resonant. These

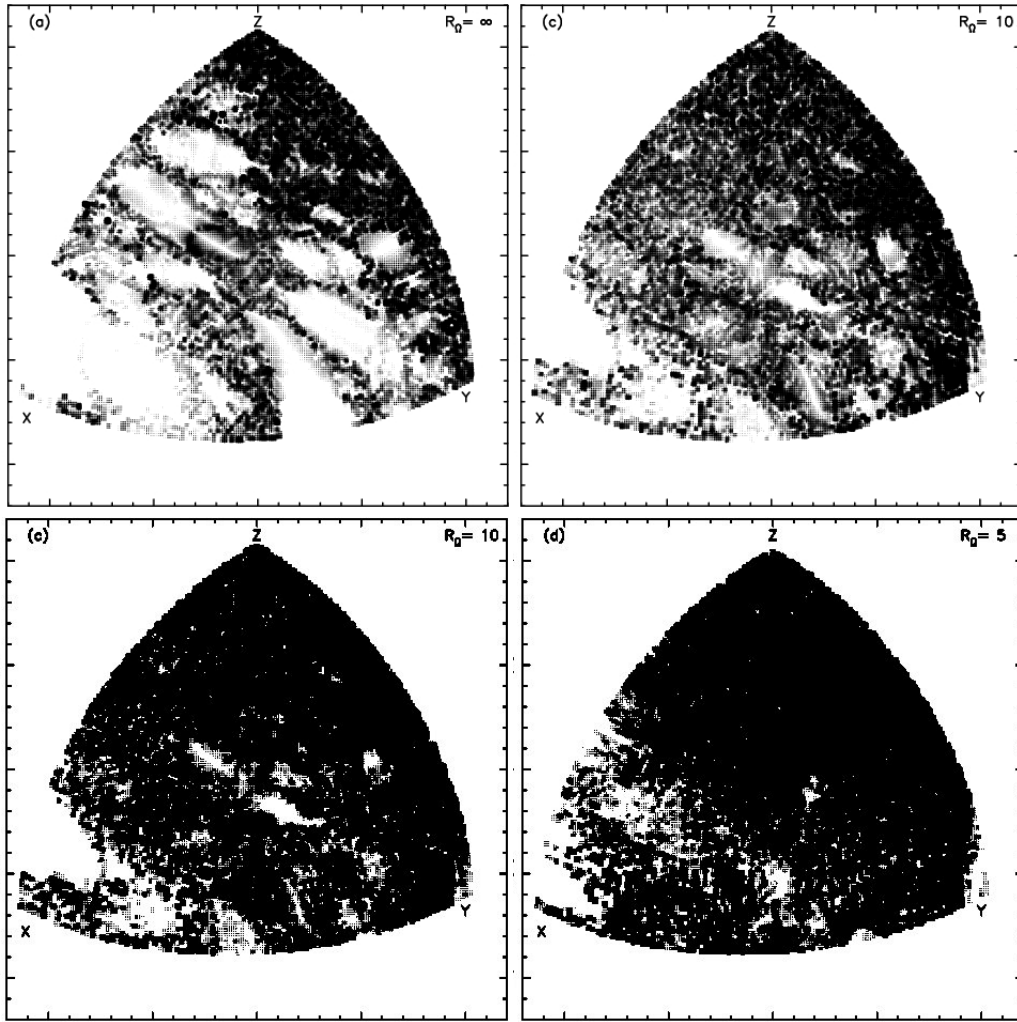


FIG. 5.— Diffusion maps of orbits launched from the box orbit start space on the 8th energy shell of a model with  $c/a = 0.5$ ,  $T = 0.58$ ,  $\gamma = 1$ , and  $M_{bh} = 0.001$ . The value of  $R_\Omega = \infty$  refers to a model with no rotation while  $R_\Omega = 40, 10$ , and  $5$  refer to the corotation radii of models with increasing pattern frequencies.

too appear to be destabilized by figure rotation. Additionally, (Gerhard & Binney 1985) predicted that orbits that are chaotic in the stationary frame should become regular in the rotating frame, but this was not seen.

The second reason for the increase in the fraction of chaotic boxlike orbits can be seen by plotting frequency maps. Frequency maps for the default model ( $c/a = 0.5$ ,  $T = 0.58$ ,  $\gamma = 1$ , and  $M_{bh} = 0$ ) show resonant orbits clustered along resonance lines, and non-resonant regular orbits and stochastic orbits scattered over the rest of the map (Figure 7(a)). The points scattered along a line with a slope of approximately unity on the right hand side of the map correspond to chaotic box orbits which lie at the separatrix boundary with a family of short-axis tubes with  $\omega_x \sim \omega_y$ .

For the slowest rotation frequency ( $R_\Omega = 40$ ), we observe the disappearance of some of the weakest resonances but the overall structure of the frequency map remains intact. As the corotation radius of the model decreases (higher rotation frequencies) the entire frequency map appears to shrink with the boundaries moving toward the bottom right toward the short-axis tube “resonance”. This is because as the pattern frequency of the model increases, each orbit experiences a centrifugal force that changes both  $\omega_x$  and  $\omega_y$ . For a small fraction of orbits that lie close to the equatorial plane of the

model with large  $y$  values, the change in orbital frequencies is large enough to convert them to resonant  $z$ -tubes (e.g., Figure 11 (top row)).

The frequency maps show the increased width of the stable resonance lines (which occur due to the envelope doubling discussed above). In addition a few new resonances appear as the pattern speed increases. The shrinking of the frequency map, the broadening of resonances, and the appearance of new resonances together contribute to a significant increase in the overlap of resonances. Resonance overlap is a well known cause of global chaos in Hamiltonian systems (Chirikov 1979) and may be thought of as occurring when several different resonances compete to trap the same orbit (BT08). This implies that even if figure rotation could allow chaotic box orbits to avoid the center as suggested by Gerhard & Binney (1985), the compression of the range of frequencies resulting from the modulation of orbit frequencies with the pattern frequency results in such significant overlap in resonant orbits that the effects of global chaos dominate the behavior of box orbits.

### 3.2. Effect of moderate figure rotation on tubelike orbits

We now explore the effect of figure rotation on tube-like orbits in the default model. The diffusion maps in Figure 8 show orbits launched from the  $Y$ - $\alpha$  start space, with the gray

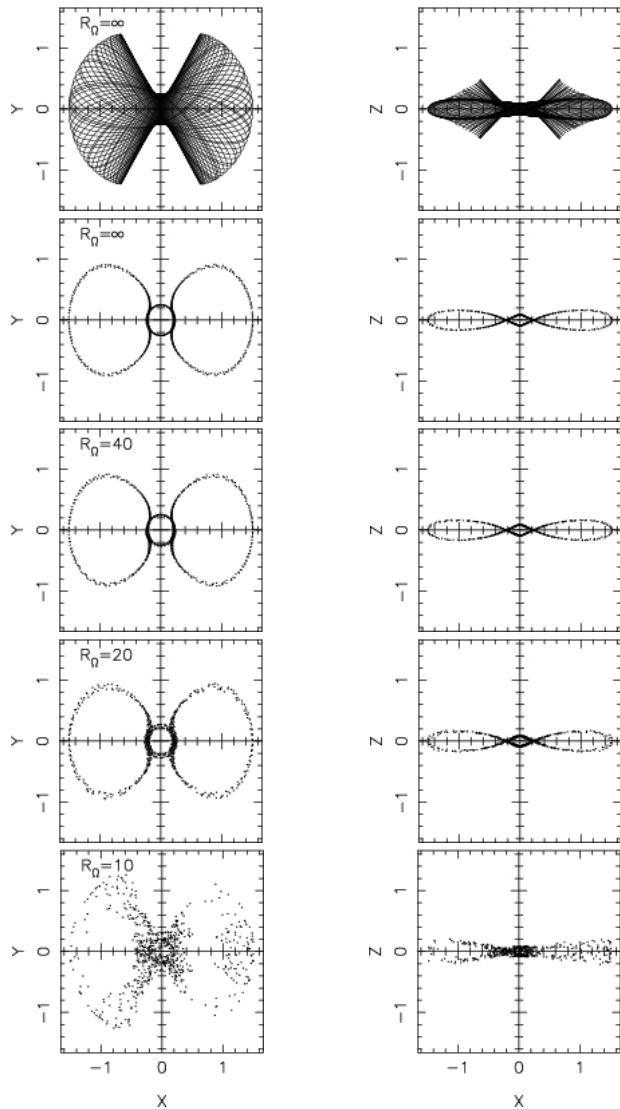


FIG. 6.— Resonant orbit associated with the  $(3,-1,-1)$  resonance. The top row shows two Cartesian projections of the orbit. The next four rows show cross sections of the orbit with the  $x$ - $y$  plane (left) and with the  $x$ - $z$  plane (right) with increasing pattern frequencies ( $R_\Omega = \infty, 40, 20,$  and  $10$  which correspond to  $R_\Omega/a_i = 24.8, 12.4,$  and  $6.2$ ).

scale representing the diffusion parameters. (Compare with Figure 3 for the locations of the major orbit families.)

As the figure rotation of the model increases, the bi-symmetry about  $\alpha \sim 150^\circ$  is broken. For  $R_\Omega = 5$ , the prograde  $z$ -tubes shrink to occupy a region  $\alpha \sim 180^\circ \pm 20^\circ$  (i.e., close to the equatorial plane of the model) but now extend to smaller  $Y$  values than in the stationary model (panel (a)). In contrast, the retrograde  $z$ -tubes now occupy a large range of  $\alpha$  values, but predominantly at large  $Y$ . As the co-rotation radius decreases, the regions occupied by long-axis ( $x$ ) -tubes also shrink. A greater portion of phase space at small values of  $Y$  associated with box orbits becomes chaotic (consistent with what was seen in Figure 4).

Binney (1981) found from stability of the analysis of closed periodic  $(1:1)$  orbits in the equatorial plane that as figure rotation increases, retrograde closed orbits become unstable in an annular region (the “Binney instability strip”) where the perpendicular frequency is resonant with the epicyclic frequency. Based on this finding, Schwarzschild (1982) erro-

neously concluded that retrograde tube orbits would become increasingly unstable with increasing figure rotation and consequently chose to largely omit them from the self-consistent models he constructed.

The decrease in the overall fraction of initial condition space occupied by the prograde  $z$ -tubes and the corresponding growth of the retrograde  $z$ -tubes appears to be in conflict with this expectation. However, we do find that at the highest pattern frequency (panel (d)), prograde  $z$ -tubes close to the equatorial plane ( $\alpha \sim 180^\circ$ ) are stable over a wider range of  $Y$  values than the retrograde variety ( $\alpha \sim 0^\circ$ ).

In the stationary model (panel (a)) the  $x$ -tubes are found symmetrically about launch angles of  $\alpha \sim 90^\circ \pm 30^\circ, 270^\circ \pm 30^\circ$  (orbits are launched perpendicular to the  $x$ - $y$  plane). However, as the pattern frequency of figure rotation increases the portion of start space occupied by  $x$ -tubes decreases and orbits with  $\alpha \lesssim 90^\circ$  and  $\alpha \gtrsim 270^\circ$  are replaced by retrograde  $z$ -tubes (at  $Y \gtrsim 0.6$ ) and box (and chaotic) orbits (at  $Y \lesssim 0.6$ ). Thus, in the more rapidly rotating models any orbit launched vertically (with no angular momentum about the  $z$ -axis) or with velocity opposite to the direction of figure rotation will “fall behind” the model. The orbit can become a retrograde  $z$ -axis tube (in the frame corotating with the figure), a box orbit, or a chaotic orbit. (Note that although some orbits are “retrograde” in the corotating frame, they could be rotating prograde when viewed from an inertial frame.)

Note that as the corotation radius decreases, inner long-axis ( $x$ ) tubes launched close to the center of the model (small  $Y$  values) become strongly chaotic, while those launched with intermediate  $Y$  values are transformed into outer long-axis tubes and exhibit the “anomalous” behavior discussed by Heisler et al. (1982) (i.e., they are tipped about the  $y$ -axis due to the Coriolis forces). The destabilization of inner long-axis tubes is also a consequence of the envelope doubling that arises due to the Coriolis forces. Figure 9 shows projections as well as planar cross sections of two inner long-axis tubes. The two columns on the left correspond to an orbit with a small pericenter radius which is destabilized, while the orbit on the right goes through a phase where it appears chaotic but is once again stable at a higher pattern frequency, although it is tipped about the  $y$ -axis and significantly flattened.

Valluri et al. (2010) showed that in triaxial  $N$ -body halos  $x$ -tubes are the second most important family after the boxes ( $\sim 85\%$ ) and constitute 11% of the orbits. They also showed that in prolate dark matter halos (the shapes most commonly found in cosmological simulations; Dubinski & Carlberg 1991; Jing & Suto 2000; Allgood et al. 2006) the fraction of long-axis tubes can be as high as 75%. Our finding that  $x$ -tubes with small pericenter radii are easily destabilized is consistent with observations by Valluri et al. (2010) that long-axis tubes with small pericenter radii are quite easily destabilized by the presence of a central point mass in self-consistent (but non-rotating)  $N$ -body models.

The discussions in this section indicate that as figure rotation increases the fraction of phase space occupied by prograde  $z$ -tubes and  $x$ -tubes (both clockwise and anti-clockwise) decreases and this decrease is accompanied by an increase in the fraction of stable retrograde  $z$ -tubes and chaotic orbits.

### 3.3. Effects of Fast Rotation

We briefly explore the behavior of orbits when the pattern frequency of figure rotation approaches that of bars. Most bars are rapidly rotating with corotation radii roughly 1–1.4 times the length of the bar (e.g., Debattista et al. 2002; Aguerri

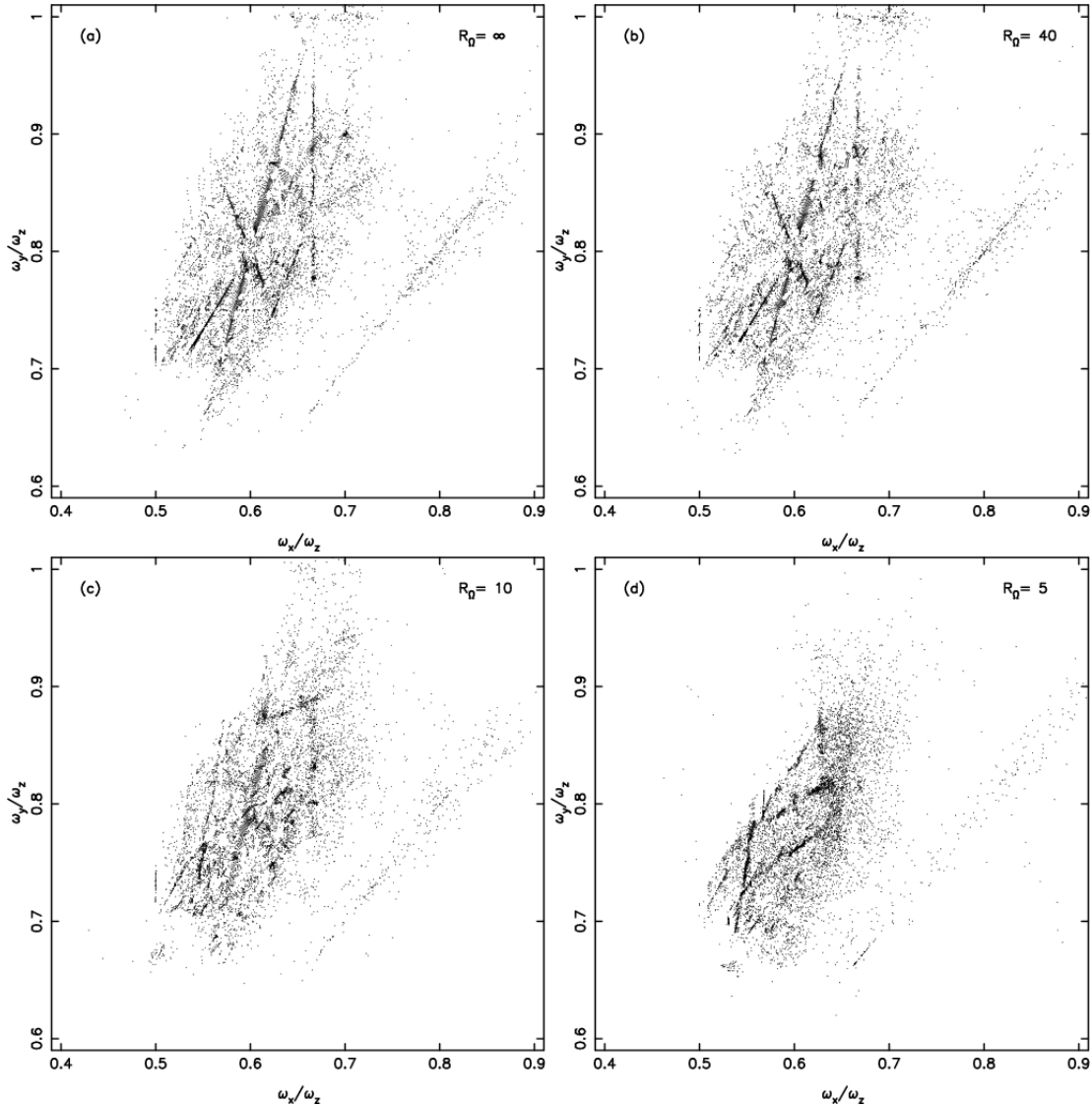


FIG. 7.— Frequency maps for box orbit start space at shell 8 in the default model ( $c/a = 0.5$ ,  $T = 0.58$ ,  $\gamma = 1$ , and  $M_{bh} = 0$ ) for a non-rotating model ( $R_\Omega = \infty$ ) and three rotating models ( $R_\Omega = 40, 10$ , and  $5$ ).

et al. 2003; Corsini 2010; Binney & Tremaine 2008).

Figure 10 shows the effect on orbits launched from the 8th energy shell in the default model with figure rotation corresponding to a corotation radius  $R_\Omega = 2$  ( $R_\Omega/a_i = 1.24$ ). Panel (a) shows the diffusion map for orbits launched from the stationary start space in the default model; in contrast with Figure 4(d) ( $R_\Omega = 5$ ), which was occupied almost entirely by chaotic boxlike orbits, at a high pattern frequency the diffusion map shows a transition to predominantly regular orbits. An inspection of the corresponding frequency map (panel (b)) reveals that the orbits no longer have box-like characteristics but instead predominantly lie along a diagonal line indicating that they are more like  $z$ -tube orbits. Panel (c) of Figure 10 shows that while a significant fraction of orbits are chaotic, the major tube families (the  $x$ -tubes and  $z$ -tubes) do persist, and stable retrograde  $z$ -tubes are again a dominant population.

Examples of some of the regular orbits launched from the box start space that appear at the highest pattern frequency are shown in the lower three rows of Figure 11. While these orbits do loop around the  $z$ -axis and therefore superficially resemble  $z$ -tubes they are in fact a distinct family more closely

resembling orbits in barred galaxies. This is not surprising since this pattern speed,  $R_\Omega/a_i = 1.24$ , is in the range of values seen in fast bars.

As mentioned previously, the normalized angular momentum  $\langle J_z/|J_z| \rangle$  is close to unity for bona fide  $z$ -tubes. However, these new loop-like orbits have a wide range of  $\langle J_z/|J_z| \rangle$  values, most of which are significantly smaller than unity. This is because although these orbits loop about the center on average in a retrograde sense, these orbits frequently make small prograde “epicycle-like” loops (instead of turning points in the stationary frame) (see left-hand plots of Figure 11. For these orbits  $\langle J_z/|J_z| \rangle$  is larger than the other two components of angular momentum, but it is smaller than unity. Our automatic orbit classifier therefore identifies these orbits as boxes and not  $z$ -tubes. These orbits are not axisymmetric in the  $x$ - $y$  plane and have elongated box-like projections in the  $x$ - $z$  plane which would be useful in the construction of self-consistent triaxial models.

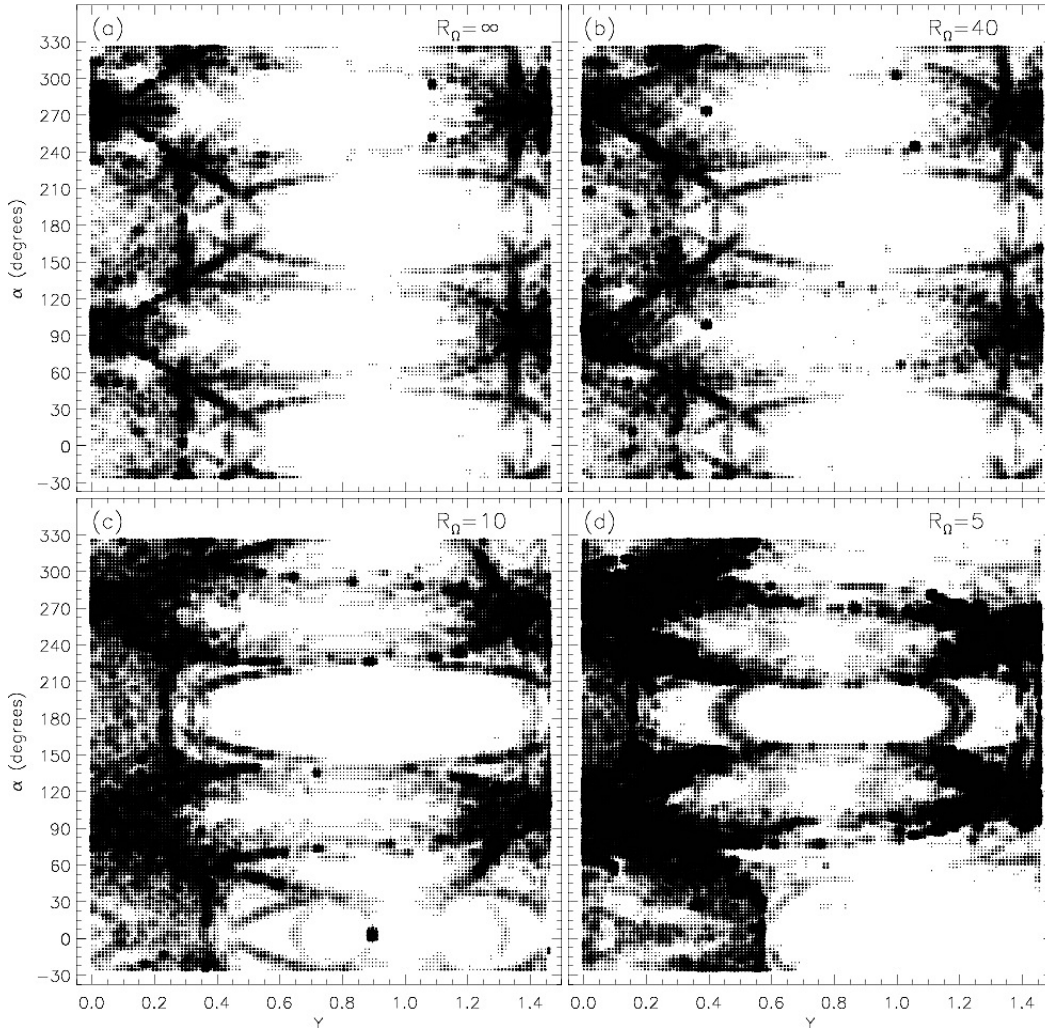


FIG. 8.— Diffusion maps for orbits launched from the  $Y$ - $\alpha$  start space in a Dehnen triaxial model (with  $c/a = 0.5$ ,  $T = 0.58$ ,  $\gamma = 1$ , and  $M_{bh} = 0$ ). Panel (a) shows the model with no rotation ( $R_\Omega = \infty$ ) while the other three panels show models with increasing pattern frequency ( $R_\Omega = 40, 10$ , and  $5$ ).

### 3.4. Dependence on radial shell

In order to draw conclusions about the orbit composition and stability of equilibrium triaxial galaxies with varying pattern speeds it is not adequate to restrict the study to orbits with a single energy (e.g., the 8th energy shell). It is important to assess how the fractions of various orbit families depend on their potential energy, in *self-consistent* models such as those constructed via Schwarzschild's orbit superposition method. Self-consistent Schwarzschild models will be constructed in a future study (Valluri 2011). In the next two subsections, we will study the properties of orbits at six different radii in a stationary model as well as in a rotating model with  $R_\Omega = 10$ . Such an assessment, while not a substitute for constructing self-consistent models, can lead to insights into properties of such models. We consider orbits in the default model for the " $Y$ - $\alpha$ " start space as well as orbits from the "stationary" start space. For the latter we consider only a model with a central point mass (representing an SMBH). Orbits launched from start spaces equipotential surfaces corresponding to shells 2, 5, 8, 10, 12, and 16 (recall that outer edge of the 16th shell encloses 80% of the total mass of the model). These shells have major axes (in units of  $a$ ) of 0.45, 0.95, 1.61, 2.22, 3.10, and 6.87, respectively. For  $R_\Omega = 10$ , the corresponding values of  $R_\Omega/a_i$  are 22.22, 10.52, 6.21, 4.50, 3.22, and 1.46. For the

16th shell, the value of  $R_\Omega/a_i = 1.46$  is approaching the value of that seen in fast bars, accounting for the increased fraction of the new family of regular loop-like orbits.

#### 3.4.1. Tubelike orbits

Figure 12 shows diffusion maps of the  $Y$ - $\alpha$  start space for the six different shells. The maps are color coded as in Figure 3(b) with black denoting box-like orbits, cyan, and blue denoting clockwise and anti-clockwise  $x$ -tubes, ochre denoting clockwise (retrograde)  $z$ -tubes and red denoting anti-clockwise (prograde)  $z$ -tubes.

The first five shells show many of the characteristics that we saw previously: box orbits and chaotic orbits dominate at small  $Y$  values in all shells. In shell 2, box orbits and inner long-axis tubes are found within the inner half of the diffusion plot and are often mildly chaotic. In the outer parts of the model (shell 16), the box orbits only occupy a small fraction of the phase space and the tube orbit families (clockwise and anti-clockwise varieties) occupy equal areas of the initial condition space. As before the various orbit families are separated by chaotic separatrix layers and in addition unstable resonances appear as dark bands in the regions occupied by  $z$ - and  $x$ -tubes.

Figure 13 shows the effect of figure rotation on the orbits

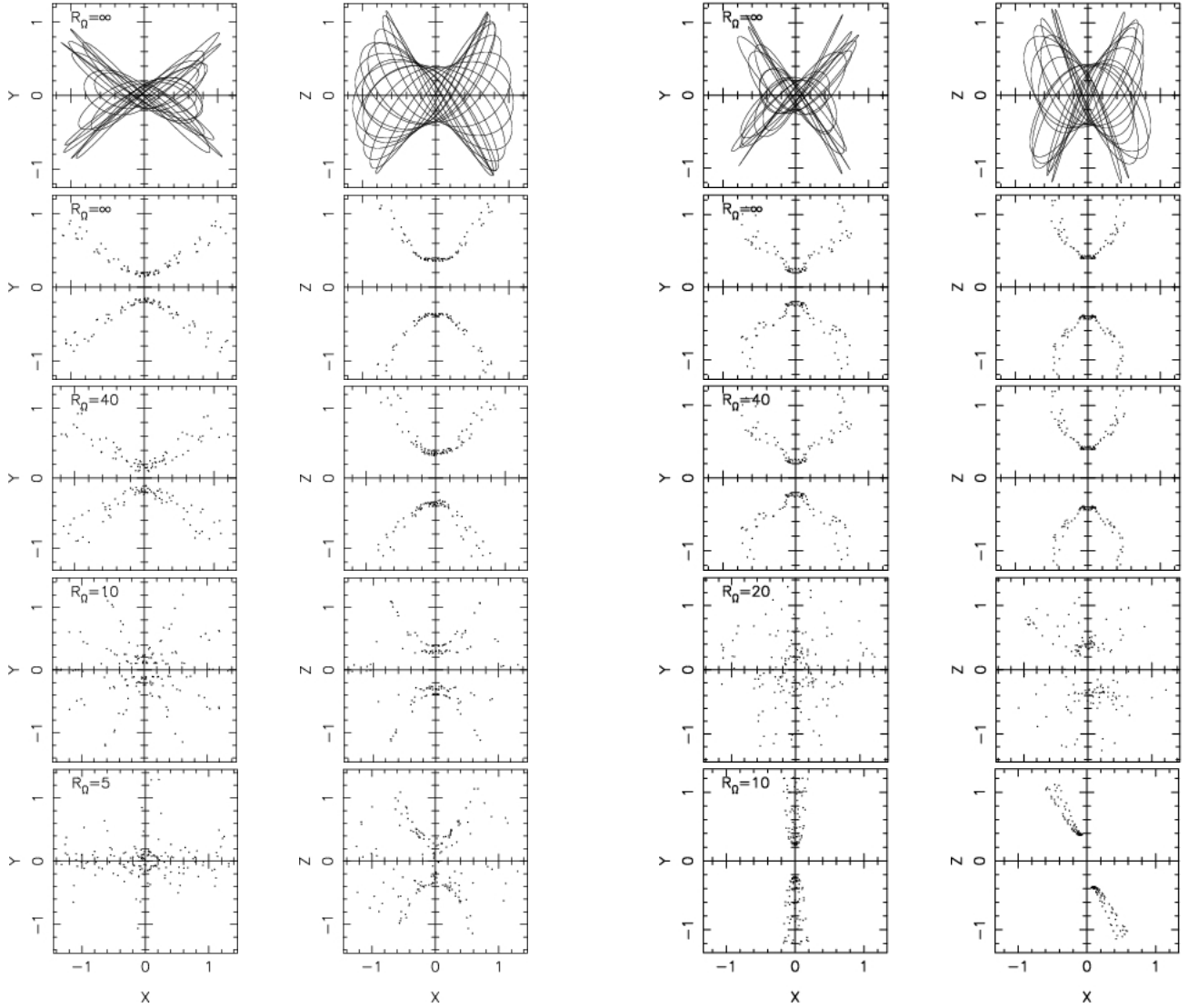


FIG. 9.— Example of two inner long-axis ( $x$ ) tube orbits. The top row shows two projections of the orbit in the  $x$ - $y$  (left) and  $x$ - $z$  (right) planes in the stationary model. The second row shows cross sections of the same orbits with the  $x$ - $y$  and  $x$ - $z$  planes. The next three rows show that the cross sections become broadened as the pattern frequency increases, becoming chaotic and/or tipped about the  $y$ -axis for higher pattern frequencies.

in Figure 12. Note that the corotation radius of  $R_\Omega = 10$  was selected because this corotation radius lies outside shell 16 ensuring that none of the shells experience the fast pattern speeds seen in Section 3.3. Only  $\sim 10\%$  of the total mass of the model lies outside a corotation radius of  $R_\Omega = 10$ .

Figure rotation produces roughly the same qualitative effects on orbits in all six radial shells although the details depend on radius: (1) the fraction of chaotic (and boxlike) orbits (black/intense color) increases relative to the non-rotating model, especially in the outer shells, (2) the fraction of  $x$ -axis tubes (blue/cyan) decreases, (3) in shell 8 and beyond the region occupied by prograde  $z$ -tubes (red) shrinks (there are no equatorial plane prograde  $z$ -tubes by shell 16 but two new bands appear around  $\alpha \sim 90^\circ, 270^\circ$ )<sup>6</sup>, and (4) the retrograde  $z$ -tubes (white regions surrounded by ochre bands) dominate.

To better quantify the effects of figure rotation on the orbit populations we computed fractions of orbits in each of the ma-

<sup>6</sup> The new bands of prograde  $z$ -tubes that appear at  $\alpha \sim 100$  and  $\alpha \sim 260$  at the outer most energy shells are classified by our automatic classifier as  $z$ -tubes but are in fact  $x$ -tubes that have been tipped about the  $y$ -axis by nearly  $90^\circ$  as predicted by (Heisler et al. 1982).

for families. As discussed previously, we use time-averaged normalized angular momentum values to distinguish between boxes,  $x$ -tubes, and  $z$ -tubes. In addition, we visually inspected 225 uniformly distributed orbits in each shell to confirm these automatic classifications and to also allow us to distinguish between inner and outer  $x$ -tubes. The results of the orbit classification are plotted in Figure 14 for the models in Figure 12 ( $R_\Omega = \infty$ ) and Figure 13 ( $R_\Omega = 10$ ). In the absence of figure rotation (left) the fractions of prograde and retrograde  $z$ -tubes are exactly the same so the ( $\times$ ) and (+) symbols overlap; at a higher pattern speed (right), the ochre curve (retrograde  $z$ -tubes) and red curve (prograde  $z$ -tubes) separate clearly showing the dominance of the retrograde family, especially at large radii. In this plot we do not distinguish between chaotic and boxlike orbits, since to do so would require setting an arbitrary “cutoff” value for the diffusion parameter at which orbits would be classified as chaotic. Most of the orbits classified as boxlike are in fact chaotic, but a large number of the tube like orbits (especially the  $x$ -axis tubes) are quite strongly chaotic as can be seen from the intensity of the blue and cyan regions in Figures 12 and 13.



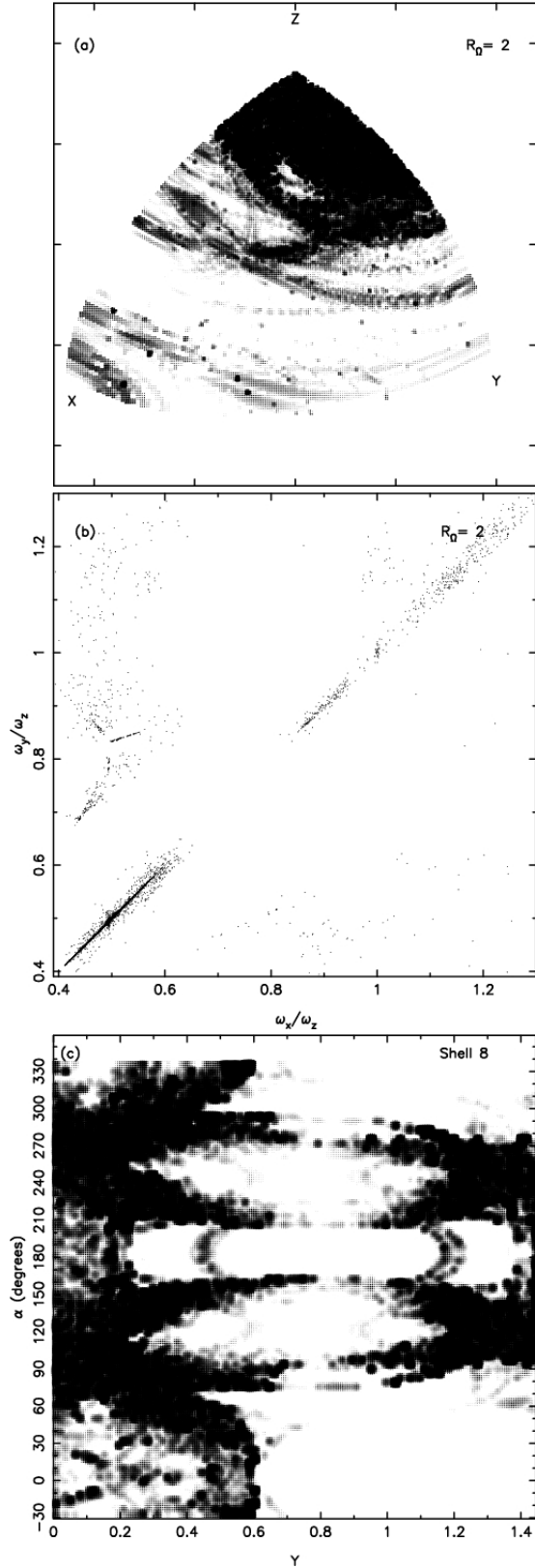


FIG. 10.— (a) Stationary start space diffusion map, (b) stationary start space frequency map, and (c)  $Y$ - $\alpha$  start space diffusion map for orbits in the 8th energy shell in models with  $c/a = 0.5$ ,  $T = 0.58$ ,  $\gamma = 1$ ,  $M_{bh} = 0$ , and  $R_\Omega = 2$  ( $R_\Omega/a_i = 1.24$ ).

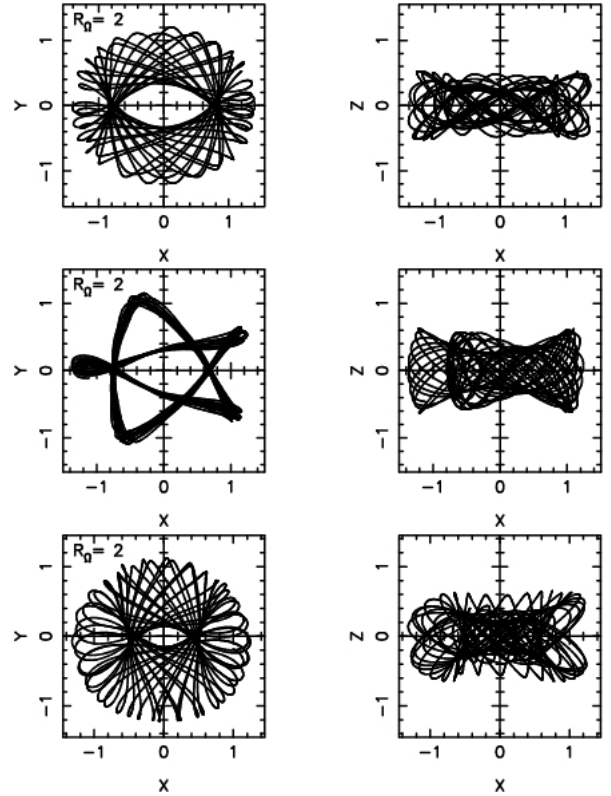


FIG. 11.— Box orbits in models with high pattern speeds are transformed to regular retrograde orbits that circulate about the  $z$ -axis and loop around the center. Top row: a retrograde short-axis tube orbit that originates close to the  $y$ -axis on the equatorial plane that first appears at moderate pattern speeds ( $R_\Omega = 10, 5$ ). Rows 2–4: examples of regular “bar-like” loop-orbits that dominate the regular orbit population of orbits launched from the “box” start space at  $R_\Omega = 2$  ( $R_\Omega/a_2 = 1.24$ ).

The figure shows that the fraction of box-like (chaotic) orbits increases slightly in the inner shells but increases significantly in the outer shells (but is as high as 40% in many shells in the rotating models). Note that in contrast, the fraction of box orbits drops with radius in the stationary model (left). The fraction of inner  $x$ -axis tubes is not very significant even in the stationary model but decreases significantly, disappearing entirely at larger radii in the rotating model. (While inner long-axis tubes do not play a significant role in maximally triaxial models, they are elongated along the major axis of the potential and are vital, in addition to box orbits, for maintaining the triaxial shape in significantly prolate models.) The outer long ( $x$ ) axis tube fraction decreases slightly at most energies, but especially at large radii. The fraction of prograde versus retrograde  $z$ -tubes remains almost unchanged in the inner two shells, but there is a significant decrease in fraction of prograde  $z$ -tubes (red curve  $+$ ) signs in the outer energy shells and a corresponding increase in the retrograde fraction (ochre curve  $\times$ ). We note that the behavior of orbits in shell 8 in response to figure rotation is broadly indicative of average behavior of orbits in different radial shells. Thus, it is reasonable to use this shell to gauge the average effect of figure rotation on the entire model, but not to predict the detailed radial structure of such galaxies.

### 3.4.2. Box-like orbits

Since box orbits are generally regarded as the most important family for supporting triaxiality, it is also necessary to study the radial dependence of their stability. The stability of

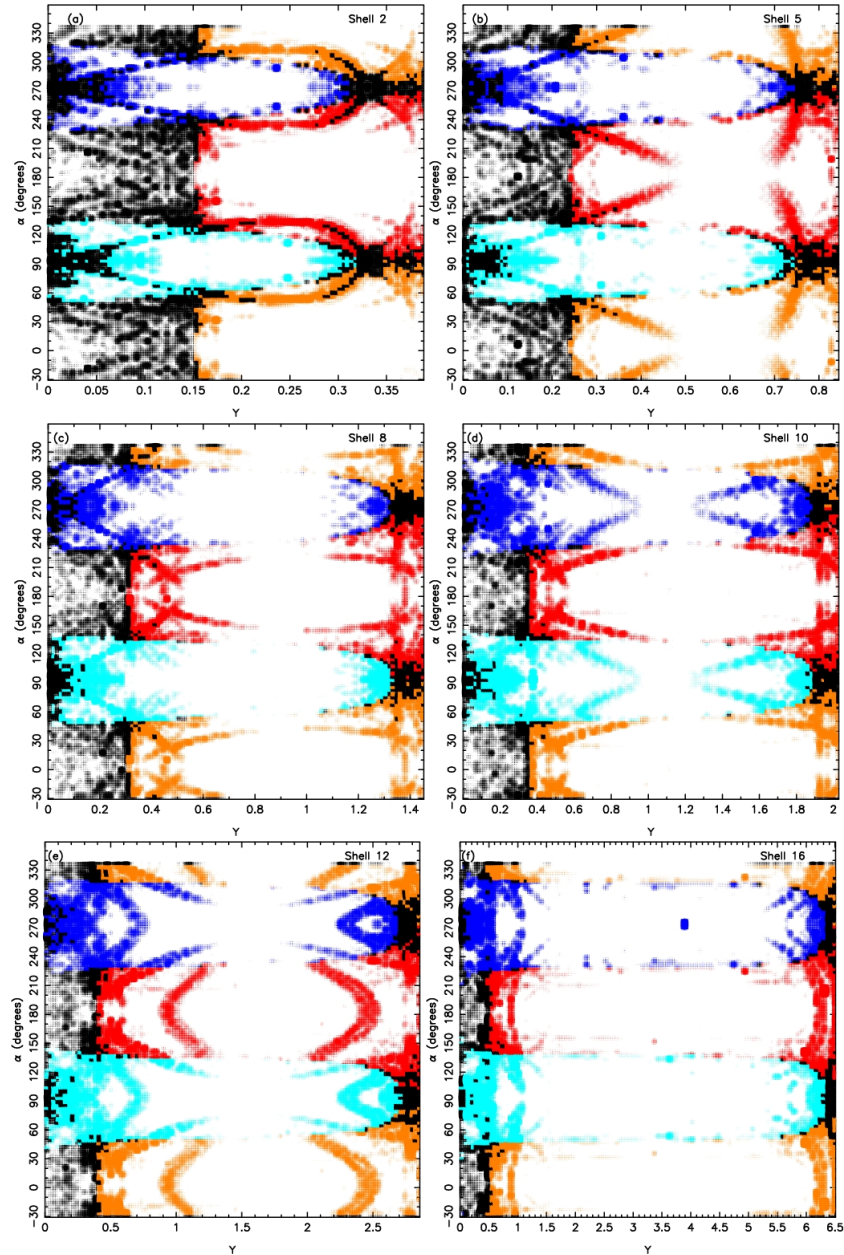


FIG. 12.— Diffusion maps on the  $Y$ - $\alpha$  start space for orbits at six different energy levels in a non-rotating model with  $(c/a = 0.5, T = 0.58, \gamma = 1, \text{ and } M_{bh} = 0)$ .

box orbits is strongly affected by chaotic scattering by a central black hole. Since SMBHs are now believed to reside at the centers of all galaxies with a significant bulge/ellipsoidal components, we now consider behavior of orbits launched from the stationary (box) start space in models with SMBHs.

Figure 15 shows diffusion maps for orbits launched from six different radial energy shells (as labeled) in the absence of figure rotation. There is a large fraction of chaotic orbits at all radii. At small and intermediate radii, there are numerous small resonant islands. In the outer two shells, there are only three larger islands associated with regular orbits and these are mostly associated with non-resonant box orbits (although some small resonant islands persist).

Figure 16 shows the effect of figure rotation ( $R_\Omega = 10$ ) on the box-like orbits in Figure 15. In the inner three shells we see that figure rotation has the effect of reducing the sizes of

the regular islands of resonant orbits that we previously discussed in Section 3.1. The disappearance of resonant islands is particularly notable in the inner four shells where the non-rotating model (Figure 15) shows numerous small islands. In the outer two shells (which are closer to the corotation radius), we see the onset of regularity associated with orbits close to the  $y$ -axis. These orbits have  $z$ -tube-like characteristics which was previously demonstrated in Figures 11 and 10.

Very near the SMBH, within its gravitational sphere of influence, motion in non-rotating triaxial galaxies is essentially regular; orbits take the form of perturbed Keplerian ellipses that gradually precess due to the torques from the stellar potential (Merritt & Vasiliev 2010). The innermost radial shell of our models contains a stellar mass  $\sim 0.05M_{gal} \approx 50M_{bh}$  and so lies well outside of the influence sphere.

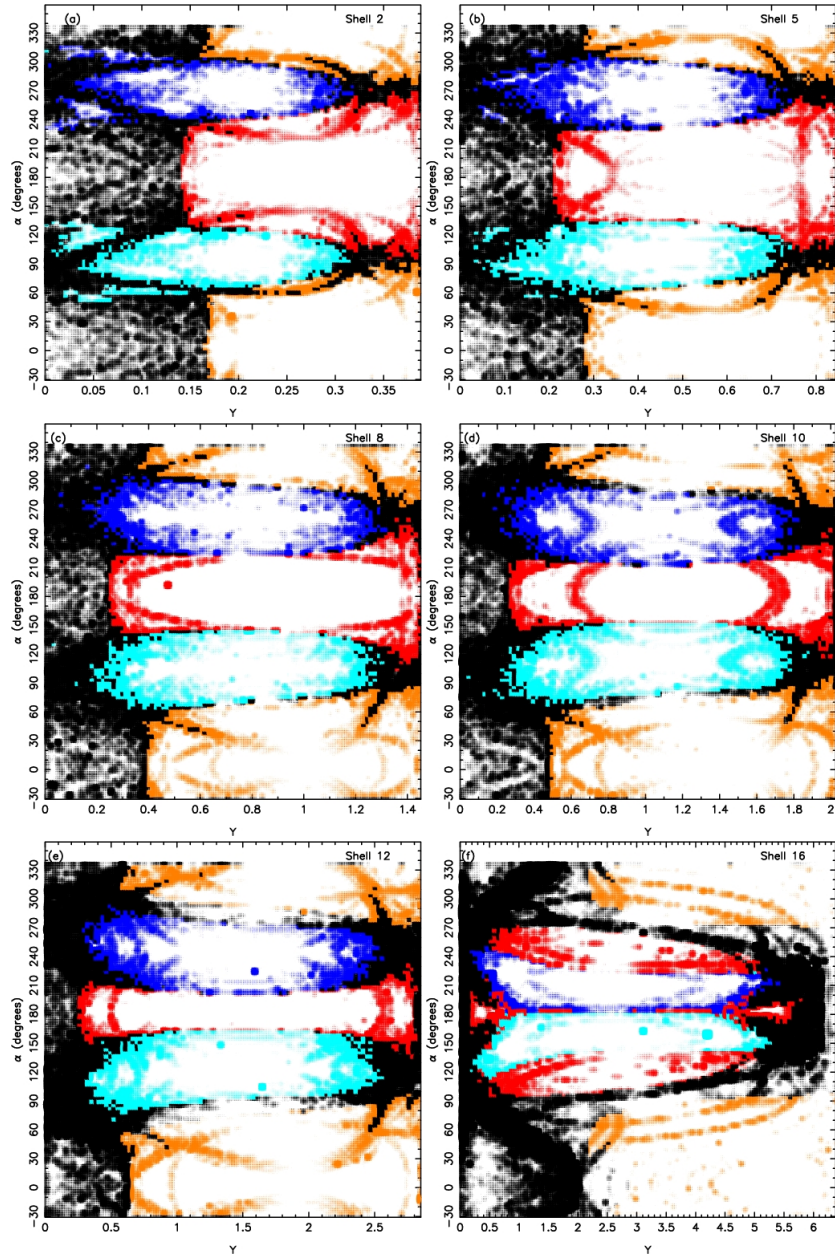


FIG. 13.— Diffusion maps on the  $Y$ - $\alpha$  start space for orbits at six different energy levels in a model with ( $c/a = 0.5$ ,  $T = 0.58$ ,  $\gamma = 1$ , and  $M_{bh} = 0$ ). For  $R_\Omega = 10$ ,  $R_\Omega/a_i$ : 22.22, 6.21, 5.98, 3.22, and 1.54 for radial shells 2, 5, 8, 10, 12, and 16, respectively.

### 3.5. The effect of varying the shape of the model

The projected shape of a galaxy on the sky depends both on its intrinsic shape (i.e., the value of  $T$  and  $c/a$ ) as well as its orientation relative to the line of sight. Although it is possible to measure only the projected shape of an individual early-type galaxy it is possible to infer the properties of the distribution of shapes from the assumption that each individual in a large sample should be randomly oriented. Using surface photometry of the apparent shapes of elliptical galaxies it has been shown that their intrinsic shapes cannot be explained if they are exclusively a population of randomly oriented oblate spheroids, but the distribution of apparent shapes is consistent with their being a population of triaxial ellipsoids (Fasano & Vio 1991; Lambas et al. 1992; Ryden 1992; Tremblay & Merritt 1995; Vincent & Ryden 2005). Observationally, it appears that the lower luminosity ellipticals tend to be flat-

ter and more consistent with disk oblate systems while the higher luminosity systems are more likely moderately oblate triaxial. Strongly prolate, perfectly oblate systems, or perfectly spherical systems are rare and the more luminous elliptical galaxies are probably oblate triaxial. The models we investigated in previous sections are close to maximally triaxial and consequently could be somewhat unrealistic. Merritt (1997) explored the range of self-consistent (non-rotating) triaxial galaxies of various shapes that could be constructed exclusively with regular orbits, in Dehnen models with  $\gamma = 2$ . He showed that the allowed range of shapes for which all orbits were regular tended to be mostly oblate and oblate triaxial with a small number of nearly prolate shapes allowed.

It is out of the scope of this paper to do a full exploration of the dependence of orbital structure on galaxy shape. However, we studied the effect of figure rotation ( $R_\Omega = 10$ ) on



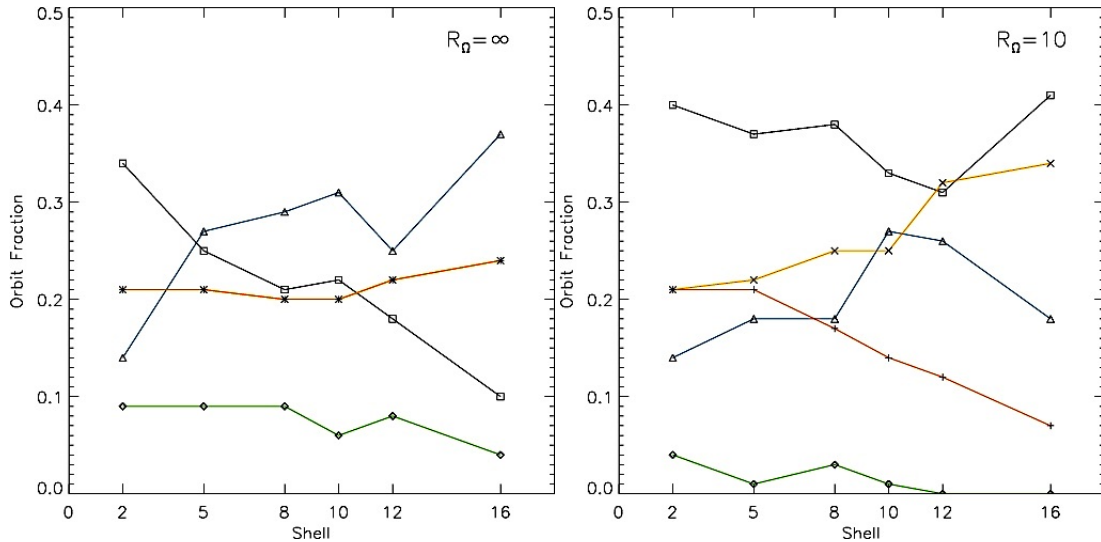


FIG. 14.— Fractions of orbits in major families as a function of radial energy shell number in the default models, left: without figure rotation and right: with figure rotation. Squares ( $\square$ ) connected by black lines denote box-like orbits (which are predominantly chaotic boxes); triangles ( $\Delta$ ) connected by blue lines denote outer  $x$ -axis tube-like orbits; diamonds ( $\diamond$ ) connected by green lines denote inner  $x$ -axis tubes; crosses ( $\times$ ) connected by red lines denote prograde  $z$ -tubes, and plus signs ( $+$ ) connected by ochre lines denote retrograde  $z$ -tubes. In the absence of figure rotation (left) the fractions of prograde and retrograde  $z$ -tubes are exactly the same so the ( $\times$ ) and ( $+$ ) symbols overlap; at a higher pattern speed (right), the ochre curve (retrograde  $z$ -tubes) and red curve (prograde  $z$ -tubes) separate clearly showing the dominance of the retrograde family, especially at large radii.

orbits launched from shell 8 in models with three additional shapes, with  $\gamma = 1$  and no black hole. Figure 17 shows the  $Y$ - $\alpha$  diffusion maps for four different models: (1) a nearly oblate model, (2) the nearly maximally triaxial model studied in previous sections, (3) a moderately triaxial model, and (4) a nearly prolate model.

In the nearly oblate model (panel (a)) the fraction of  $x$ -axis tubes is insignificantly small, being almost entirely replaced by  $z$ -tubes. The few surviving  $x$ -tubes are outer long-axis tubes. Box orbits continue to occupy only a small fraction of this start space. This is the only rapidly rotating model in which there is not a large difference between the prograde and retrograde short-axis tube orbit fractions (retrograde fraction=0.42, prograde fraction=0.35). The maximally triaxial model in panel (b) has a larger fraction of chaotic orbits than models of any other shape. The moderately triaxial model (panel (c)) has a significant fraction of  $z$ -axis tubes (especially retrograde ones) and a moderate fraction of long-axis ( $x$ ) tubes. Almost all the long-axis tubes are associated with anomalous orbits and the few that show characteristics of inner long-axis tubes are mildly chaotic. Most of the box orbits in the model are quite stable. Finally, the nearly prolate model (panel (d)) is dominated by retrograde  $z$ -axis tubes while the region occupied by prograde  $z$ -tubes is now entirely occupied by chaotic orbits. Box orbits and  $x$ -tubes are found in smaller numbers and some are moderately chaotic.

Admittedly, it is dangerous to draw conclusions about the shape distributions of self-consistent galaxy models with figure rotation, from looking at the populations of orbits in a selected number of start spaces. However, our analysis shows that orbit populations evolve slowly and systematically within an individual model (with varying  $\alpha$ ,  $Y$ , and radial shell), as well as with the shape of the figure and the degree of figure rotation. In particular we see that in models with a range of shapes, stable short-axis tubes with retrograde motion are the dominant population in the start space. At fast pattern speeds, box orbits are also replaced by retrograde loop-like orbits that circulate about the  $z$ -axis. The dominance of retrograde  $z$ -tubes at moderate to fast pattern speeds suggests that these

orbits are very likely to be important in self-consistent triaxial galaxies.

#### 4. SUMMARY AND DISCUSSION

We have investigated the effects of figure rotation on the orbital structure of a family of triaxial galaxy models that provide an accurate representation of the luminosity profiles of elliptical galaxies. Most of our study is restricted to models that are close to maximally triaxial with  $c/a = 0.5$ ,  $T = 0.58$ , with shallow cusps of  $\gamma = 1$ . Rotation of the figure was assumed to be about the short axis.

Our major results are summarized below.

1. As figure rotation increases, the fraction of initial condition space occupied by prograde  $z$ - and  $x$ -tube orbits (both clockwise and anti-clockwise) decreases. The fraction of stable retrograde  $z$ -tubes and chaotic orbits correspondingly increases.
2. Almost all regular box-like orbits in realistic triaxial potentials with central cusps and/or black holes are associated with resonant orbits. The Coriolis forces in the rotating frame of a triaxial potential destabilize these near-resonant box orbits as well as inner long-axis tube orbits, by thickening them enough to drive them into the center. The outer long-axis tubes are also slightly destabilized by figure rotation but less than the inner long-axis tubes. Box orbits are further destabilized because the modulation of the orbital frequencies by the rotational frequency results in a shrinking in the overall range of orbital frequencies, and therefore in significant resonance overlap. Orbits that are chaotic in the stationary model are not in general stabilized unless they occupy very special regions in phase space.
3. Over a wide range of pattern speeds there is little evidence that orbits that are chaotic in the stationary model are stabilized in the rotating model due to avoidance of the center. At fairly rapid rotation speeds, a small region close to the  $y$ -axis that is occupied by chaotic

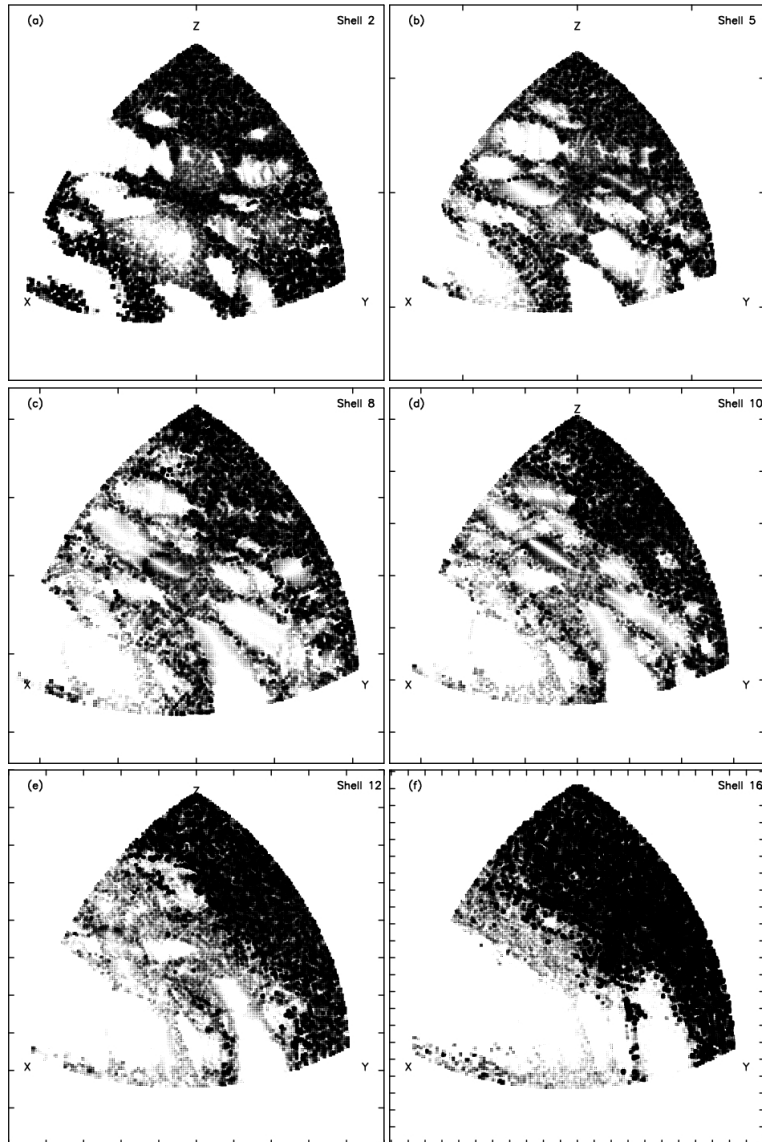


FIG. 15.— Diffusion maps on the box start space for orbits at six different radial energy shells (as labeled) in a model with ( $c/a = 0.5$ ,  $T = 0.58$ , and  $\gamma = 1$ ). The model has a central black hole of  $M_{bh} = 0.001$  and no figure rotation.

box orbits in the stationary model is indeed stabilized by figure rotation as predicted by Gerhard & Binney (1985). However, this stabilization is due to a complete transformation of the orbital characteristics from box-like to tube-like, rather than due to deflection of the chaotic box orbit around the destabilizing center. At even higher pattern speeds (Figure 10)  $R_{\Omega}/a_i \lesssim 3$  box-like orbits begin to show a sudden transformation to a new family of retrograde loop-like orbits similar to those seen in rapidly rotating bars. These orbits loop around the  $z$ -axis in an overall retrograde sense, but execute small “epicycle”-like prograde motions at points in the orbit that correspond to stationary points in the non-rotating model.

4. A surprising result of our study is that as the pattern speed  $\Omega_p$  increases there is a decrease in the overall fraction of prograde short-axis tubes which are increasingly replaced by the retrograde variety. Prograde short-axis tubes only persist when launched at angles

$\sim \pm 20^\circ$  from the equatorial plane of the model. Orbits launched at larger angles to the equatorial plane have lower angular momenta about the short axis at a given energy, and consequently tend to “fall behind” the figure and become retrograde as it rotates past them.

5. There is a fairly strong dependence of the changes in the behavior of orbits on the radial energy level from which they are launched. (1) The fraction of inner  $x$ -tubes decreases slightly at all radii, essentially disappearing at large radii. (2) The fraction of outer  $x$ -tubes also decreases at all radii. (3) The fraction of retrograde  $z$ -tubes increases and is accompanied by a decrease in the fraction of prograde  $z$ -tubes. (4) There is an overall increase in the fraction of chaotic/box-like orbits at all radii, but the increase is most significant at intermediate and large radii.
6. As the shape of the triaxial figure changes, the orbital populations at shell 8 (roughly the half-mass radius)

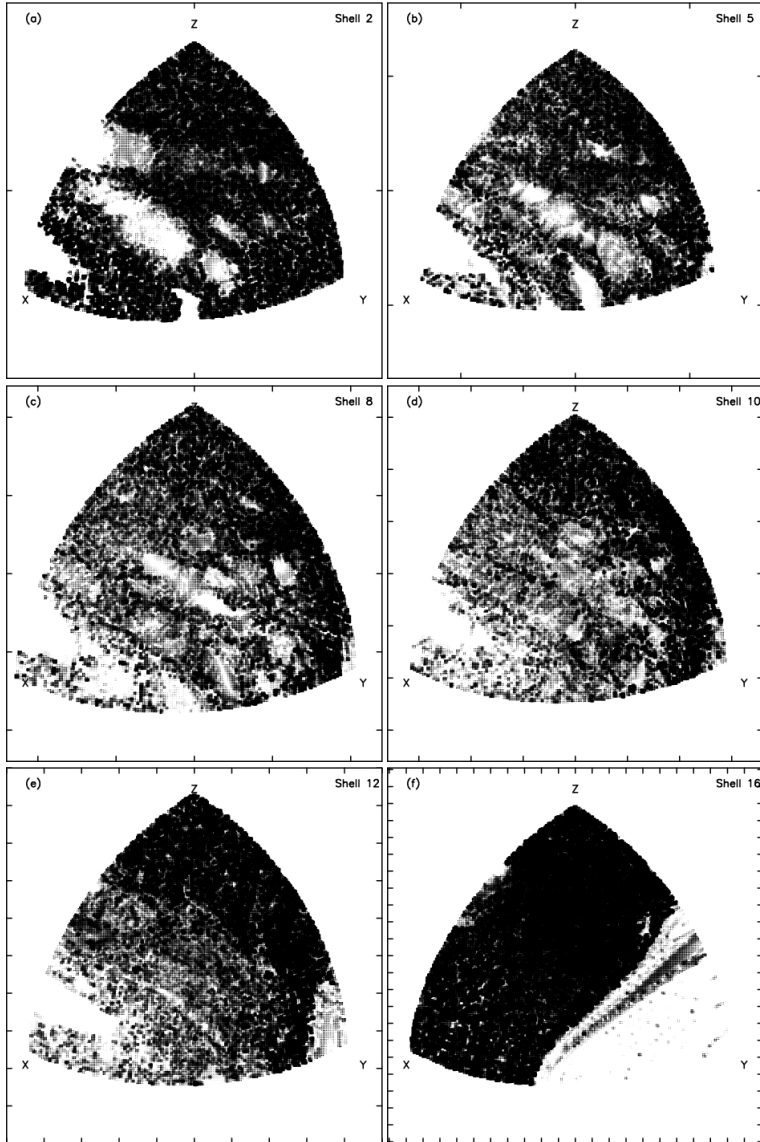


FIG. 16.— Diffusion maps on the box start space for orbits at six different energy levels in a model with  $(c/a = 0.5, T = 0.58, \gamma = 1, \text{ and } M_{bh} = 0.001)$  with co-rotation radius of  $R_\Omega = 10$ . For shells 2,5, 8,10,12, and 16, respectively, this pattern speed corresponds to  $R_\Omega/a_i : 22.22, 10.52, 6.21, 4.5, 3.22, \text{ and } 1.46$ .

vary. Yet in all cases with figure rotation (with  $R_\Omega = 10$ ) retrograde  $z$ -tubes are the most robust and stable population. The fraction of chaotic orbits is lower than in the maximally triaxial models.

It has been known for three decades, since the work of Schwarzschild (1982), that self-consistent triaxial equilibria can be constructed if the triaxial figure is rotating slowly. Schwarzschild’s study was restricted to galaxies with central cores; our study of orbits in more realistic triaxial models supports the view that galaxies with slow figure rotation have a large fraction of stable “triaxial orbit families” such as boxes and long-axis tubes which can be used to construct stable triaxial models. We find, however, that as the pattern speed of figure rotation increases, these two important families (stable resonant boxes and long-axis tubes) become increasingly unstable, due to the effects of envelope doubling. When the pattern frequency is between  $\Omega_p \simeq 3\text{-}30 \text{ km s}^{-1} \text{ kpc}^{-1}$  (for an

elliptical galaxy of scale radius 5 kpc and mass  $5 \times 10^{11} M_\odot$ ), figure rotation produces a sufficiently large amount of global chaos to make it unlikely that equilibrium triaxial models with such pattern speeds would exist – at least, if one assumes that a significant fraction of elongated regular orbits are required. At higher pattern frequencies, comparable to those of fast bars, the phase space associated with box-like orbits becomes stable once again, although the orbits now resemble loops found in fast bars.

Pattern speeds of real triaxial galaxies and dark-matter halos are poorly constrained. We explored a range of values for figure rotation motivated by theoretical measurements of pattern speeds of dark matter halos arising from cosmological simulations (Bailin & Steinmetz 2004; Bryan & Cress 2007) as well as one claimed observational measurement of rotation of a triaxial dark matter halo with a pattern speed in NGC 2915 (Bureau et al. 1999) and an early-type galaxy NGC 2794 (Jeong et al. 2007). The shape assumed for the rigid triaxial dark matter halo potential in the model for NGC



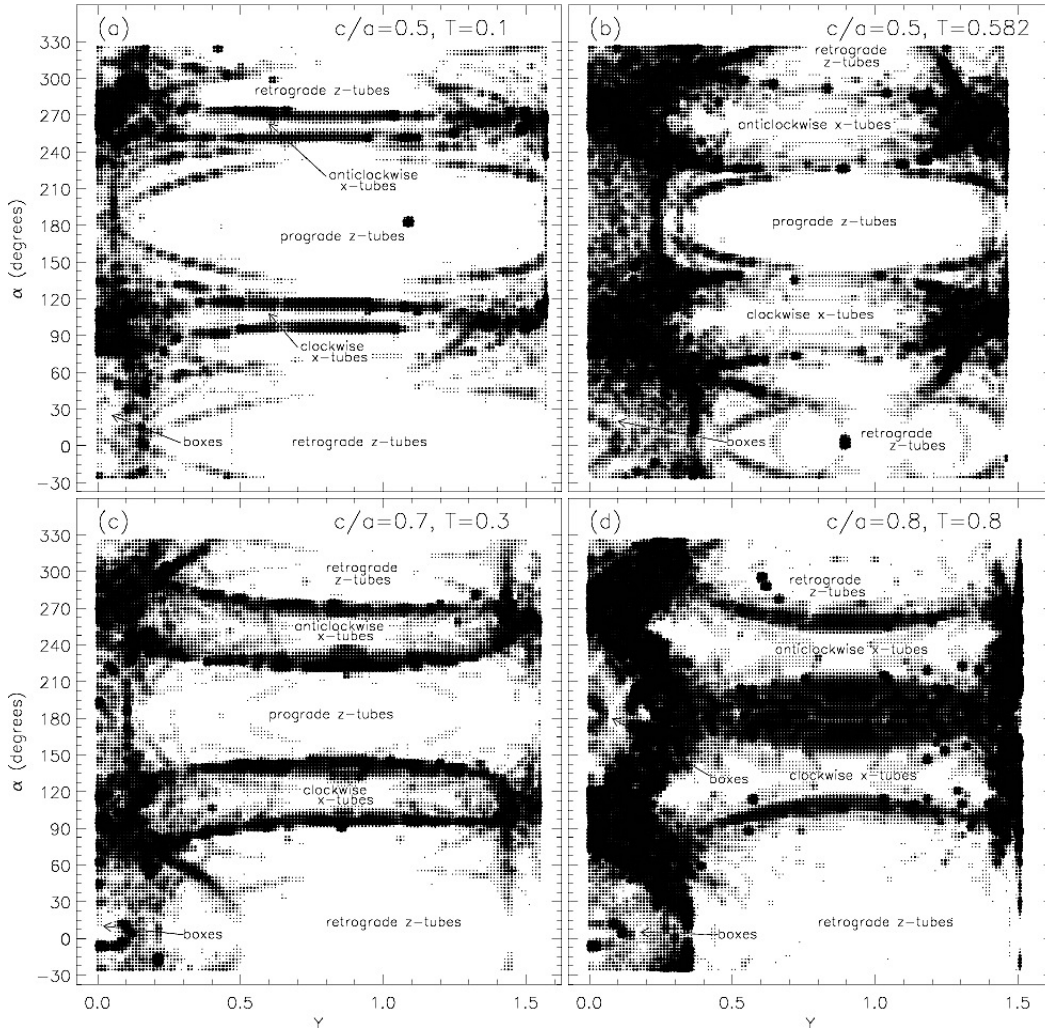


FIG. 17.— Effect of varying the shape of the galaxy on the orbit population is seen in  $Y$ - $\alpha$  diffusion maps for models with ( $\gamma = 1$  and  $R_{\Omega} = 10$ ). Panels correspond to models with various shapes as indicated by values of  $c/a$  and  $T$ . The model (a) is nearly oblate, (b) is nearly maximally triaxial, (c) is moderately triaxial, and (d) is nearly prolate. The different orbit families are clearly separated by stochastic separatrix layers.

2915 (Bekki & Freeman 2002) ( $c/a = 0.6, T = 0.56$ ) is close to our default model shape ( $c = 0.5, T = 0.58$ ). Our study suggests that the pattern speed of  $\sim 7 \pm 1 \text{ km s}^{-1} \text{ kpc}^{-1}$  required to produce the extended spiral features in this galaxy is adequate to significantly destabilize the two major families that sustain the high density along the major axis, namely, the box orbits (predominantly associated with resonances) as well as the inner long-axis tubes. This does not imply that the spiral arms in this galaxy are not generated by tidal torques from a triaxial halo but does suggest that the halo is unlikely to be as strongly triaxial as assumed by these authors. A rapidly rotating prolate-triaxial halo (predicted by cosmological  $N$ -body simulations, Dubinski & Carlberg 1991; Jing & Suto 2000; Allgood et al. 2006) is also unlikely, because inner long-axis tubes, which are important in such models (Valluri et al. 2010), are easily destabilized by large pattern speeds.

If the orbits that are required to construct triaxial galaxies, namely, the boxes and inner long-axis tubes, become highly chaotic (or disappear entirely) at intermediate pattern speeds, they are less elongated than necessary to construct self-consistent galaxies (Merritt & Valluri 1996). This places additional constraints on both the range of shapes as well as the range of pattern speeds of real elliptical galaxies.

While we did not investigate barred galaxies, our study of a few cases with rapid rotation suggests that in addition to the limited range of shapes that elliptical galaxies can assume, stable galaxies can only have two ranges of figure rotation – very slow (with rotation periods  $T_p \gtrsim 5 \times 10^9 \text{ yr}$ ) or very fast ( $T_p \lesssim 2 \times 10^8 \text{ yr}$ ).

Since some of the orbits in models with rapid figure rotation can be quite different from those in models with slow figure rotation, the implications of our studies could also have consequences for galaxy and black hole scaling relations. All existing stellar dynamical measurements of SMBH masses in barred galaxies (e.g., NGC 1023, NGC 3384, NGC 4151) assume that the dynamics in the central region is unaffected by the presence of a large-scale bar, and consequently these systems are modeled as axisymmetric. It has been argued recently that the “black hole fundamental plane” may in fact be an artifact of the dependence of the  $M_{bh} - \sigma$  scaling relation on host morphology (Graham 2008b; Hu 2008), and in particular could be a consequence of the fact that barred galaxies appear to be offset from the  $M_{bh} - \sigma$  relation for non-barred galaxies. In addition to measurement errors in the velocity dispersion parameter  $\sigma$  that arise from large scale streaming motions in the bar (Graham 2008a), neglecting figure rotation could also

lead to errors in  $M_{bh}$ .

There are very limited observational prospects for measuring the pattern speeds of individual triaxial galaxies and dark matter halos. Measurements have only been possible where there is evidence of an extended disk-like component in which resonance patterns have been excited by the figure rotation or when the Tremaine–Weinberg method is applicable. Increasing the number of observational measurements of pattern speeds in individual galaxies is likely to be challenging. Our study of the behavior of orbits suggests that triaxial elliptical structures may have only two ranges of pattern speeds.

However, it is possible that pattern speeds of elliptical galaxies may be correlated in a statistical sense with observable measures of angular momentum content such as the  $\lambda_R$  parameter used to separate galaxies into slow and fast rotators (Emsellem et al. 2007). Certainly, a similar correlation has been found between the pattern speeds and spin parameter  $\lambda$

(Peebles 1969) of cosmological dark matter halos (Bailin & Steinmetz 2004). Further studies of self-consistent models are in progress (Valluri 2011) and will shed light on both the ranges of pattern speeds for which self-consistent equilibrium triaxial galaxies exist, as well as the observable properties.

#### ACKNOWLEDGMENTS

This work formed A.D.’s undergraduate Honors thesis at the University of Michigan.

M.V. and A.D. were supported by NSF Grant AST-0908346. D.M. is supported by Grants AST-0807910 (NSF) and NNX07AH15G (NASA). M.V. thanks Victor Debattista for detailed comments on an earlier version of this paper and for clarifying numerous properties of orbits in barred galaxies. MV also thanks Jeremy Bailin for discussions on figure rotation in cosmological dark matter halos.

#### REFERENCES

- Adams, F. C., Bloch, A. M., Butler, S. C., Druce, J. M., & Ketchum, J. A. 2007, *ApJ*, 670, 1027
- Aguerri, J. A. L., Debattista, V. P., & Corsini, E. M. 2003, *MNRAS*, 338, 465
- Allgood, B., Flores, R. A., Primack, J. R., Kravtsov, A. V., Wechsler, R. H., Faltenbacher, A., & Bullock, J. S. 2006, *MNRAS*, 367, 1781
- Bailin, J., & Steinmetz, M. 2004, *ApJ*, 616, 27
- , 2005, *ApJ*, 627, 647
- Bekki, K., & Freeman, K. C. 2002, *ApJ*, 574, L21
- Binney, J. 1981, *MNRAS*, 196, 455
- Binney, J., & Spergel, D. 1982, *ApJ*, 252, 308
- Binney, J., & Tremaine, S. 2008, *Galactic Dynamics* (2nd ed.; Princeton, NJ: Princeton Univ. Press)
- Bois, M., et al. 2010, *MNRAS*, 406, 2405
- Bryan, S. E., & Cress, C. M. 2007, *MNRAS*, 380, 657
- Bureau, M., Freeman, K. C., Pfützer, D. W., & Meurer, G. R. 1999, *AJ*, 118, 2158
- Cappellari, M., et al. 2007, *MNRAS*, 379, 418
- Chirikov, B. V. 1979, *Phys. Rep.*, 52, 263
- Corsini, E. M. 2010, arXiv e-prints
- de Zeeuw, T. 1985, *MNRAS*, 216, 273
- de Zeeuw, T., & Merritt, D. 1983, *ApJ*, 267, 571
- Debattista, V. P., Corsini, E. M., & Aguerri, J. A. L. 2002, *MNRAS*, 332, 65
- Debattista, V. P., Moore, B., Quinn, T., Kazantzidis, S., Maas, R., Mayer, L., Read, J., & Stadel, J. 2008, *ApJ*, 681, 1076
- Dehnen, W. 1993, *MNRAS*, 265, 250
- Dubinski, J. 1994, *ApJ*, 431, 617
- Dubinski, J., & Carlberg, R. G. 1991, *ApJ*, 378, 496
- Dubinski, J., & Chakrabarty, D. 2009, *ApJ*, 703, 2068
- Emsellem, E., et al. 2007, *MNRAS*, 379, 401
- Fasano, G., & Vio, R. 1991, *MNRAS*, 249, 629
- Ferrarese, L., & Merritt, D. 2000, *ApJ*, 539, L9
- Gebhardt, K., Richstone, D., Ajhar, E. A., Lauer, T. R., Dressler, A., Faber, S. M., Grillmair, C., & Tremaine, S. 1996, *AJ*, 112, 105
- Gebhardt, K., et al. 2000, *ApJ*, 539, L13
- Gerhard, O. E., & Binney, J. 1985, *MNRAS*, 216, 467
- Graham, A. W. 2008a, *ApJ*, 680, 143
- , 2008b, *PASA*, 25, 167
- Harier, E., Norsett, S. P., & Wanner, G. 1993, *Solving Ordinary Differential Equations. I. Nonstiff Problems*, 2nd edn., Springer Series in Computational Mathematics, (Berlin: Springer)
- Häring, N., & Rix, H.-W. 2004, *ApJ*, 604, L89
- Harsoula, M., & Kalapotharakos, C. 2009, *MNRAS*, 394, 1605
- Heiligman, G., & Schwarzschild, M. 1979, *ApJ*, 233, 872
- Heisler, J., Merritt, D., & Schwarzschild, M. 1982, *ApJ*, 258, 490
- Hu, J. 2008, *MNRAS*, 386, 2242
- Jeong, H., Bureau, M., Yi, S. K., Krajnović, D., & Davies, R. L. 2007, *MNRAS*, 376, 1021
- Jesseit, R., Cappellari, M., Naab, T., Emsellem, E., & Burkert, A. 2009, *MNRAS*, 397, 1202
- Jing, Y. P., & Suto, Y. 2000, *ApJ*, 529, L69
- Kandrup, H. E., & Mahon, M. E. 1994, *Phys. Rev. E*, 49, 3735
- Kazantzidis, S., Kravtsov, A. V., Zentner, A. R., Allgood, B., Nagai, D., & Moore, B. 2004, *ApJ*, 611, L73
- Lambas, D. G., Maddox, S. J., & Loveday, J. 1992, *MNRAS*, 258, 404
- Laskar, J. 1990, *Icarus*, 88, 266
- Lauer, T. R., Tremaine, S., Richstone, D., & Faber, S. M. 2007, *ApJ*, 670, 249
- Lichtenberg, A. J., & Lieberman, M. A. 1992, *Regular and Chaotic Motion* (Applied Mathematical Sciences; New York: Springer)
- Martinet, L., & Udry, S. 1990, *A&A*, 235, 69
- Meidt, S. E., Rand, R. J., Merrifield, M. R., Debattista, V. P., & Shen, J. 2008, *ApJ*, 676, 899
- Merritt, D. 1997, *ApJ*, 486, 102
- Merritt, D., & Fridman, T. 1996, *ApJ*, 460, 136
- Merritt, D., & Quinlan, G. D. 1998, *ApJ*, 498, 625
- Merritt, D., & Valluri, M. 1996, *ApJ*, 471, 82
- , 1999, *AJ*, 118, 1177
- Merritt, D., & Vasiliev, E. 2010, arXiv e-prints
- Miralda-Escude, J., & Schwarzschild, M. 1989, *ApJ*, 339, 752
- Patsis, P. A., Skokos, C., & Athanassoula, E. 2002, *MNRAS*, 337, 578
- Peebles, P. J. E. 1969, *ApJ*, 155, 393
- Pfenniger, D., & Friedli, D. 1991, *A&A*, 252, 75
- Poon, M. Y., & Merritt, D. 2002, *ApJ*, 568, L89
- , 2004, *ApJ*, 606, 774
- Ryden, B. 1992, *ApJ*, 396, 445
- Schwarzschild, M. 1982, *ApJ*, 263, 599
- , 1993, *ApJ*, 409, 563
- Siopis, C., & Kandrup, H. E. 2000, *MNRAS*, 319, 43
- Skokos, C., Patsis, P. A., & Athanassoula, E. 2002a, *MNRAS*, 333, 847
- , 2002b, *MNRAS*, 333, 861
- Tremaine, S., Richstone, D. O., Byun, Y., Dressler, A., Faber, S. M., Grillmair, C., Kormendy, J., & Lauer, T. R. 1994, *AJ*, 107, 634
- Tremaine, S., & Weinberg, M. D. 1984, *ApJ*, 282, L5
- Tremblay, B., & Merritt, D. 1995, *AJ*, 110, 1039
- Tsuchiya, T., Gouda, N., & Yamada, Y. 1993, *Prog. of Theor. Phys.*, 89, 793
- Udry, S. 1991, *A&A*, 245, 99
- Udry, S., & Pfenniger, D. 1988, *A&A*, 198, 135
- Valluri, M. 1999, in *ASP Conf. Ser.*, Vol. 182, *Galaxy Dynamics - A Rutgers Symposium*, ed. D. R. Merritt, M. Valluri, & J. A. Sellwood, (San Francisco, CA: ASP), 195
- Valluri, M. 2011, in preparation
- Valluri, M., Debattista, V. P., Quinn, T., & Moore, B. 2010, *MNRAS*, 403, 525
- Valluri, M., & Merritt, D. 1998, *ApJ*, 506, 686
- van Albada, T. S., Kotanyi, C. G., & Schwarzschild, M. 1982, *MNRAS*, 198, 303
- van den Bosch, R. C. E., & de Zeeuw, P. T. 2010, *MNRAS*, 401, 1770
- van den Bosch, R. C. E., van de Ven, G., Verolme, E. K., Cappellari, M., & de Zeeuw, P. T. 2008, *MNRAS*, 385, 647
- Vincent, R. A., & Ryden, B. S. 2005, *ApJ*, 623, 137